ORIGINAL ARTICLE

Risk assessment of confined unreinforced masonry buildings based on FEMA P-58 methodology: a case study—school buildings in Tehran

Mohammad Yekrangnia[1] · Ali Bakhshi[2] · **Mohammad Ali Ghannad[2] · Mahdi Panahi[3]**

Abstract

Seismic performance of a representative single-story confined unreinforced masonry school building in Tehran, Iran is evaluated by means of incremental dynamic analyses according to FEMA P-58 framework. For this purpose, fragility curves are derived for each of the constituent walls of the building. The in-plane behavior of the walls is considered only. Both flexible and rigid diaphragm conditions are investigated. For comparison purposes, the corresponding unconfined building exactly duplicating the considered confined unreinforced masonry building is also studied. In order to analyze the effects of near-source seismic actions on the performance of masonry buildings, two separate far-field and near-field ground motion sets containing 326 records are used. By utilizing the results of the incremental dynamic analyses and the available data of unreinforced masonry school buildings in Tehran, a scenario-based risk assessment of this type of school buildings is performed considering all three adjacent faults for three different earthquake magnitudes. Considerable performance improvement is achieved by providing confinement to the walls which leads to over $100 million reduction in the damage costs for masonry school buildings in Tehran. Also, significant reduction in seismic vulnerability, especially for unconfined masonry buildings, is observed by providing the roof with more rigidity. The findings in this study can be of direct use for disaster management of masonry school buildings in Tehran and similar cities.

Keywords Unreinforced masonry buildings · Fragility curves · Life-cycle cost analysis · Risk assessment

1 Introduction

Generally speaking, masonry buildings are classified into unreinforced and reinforced; the latter usually benefit from horizontal and vertical steel bars which significantly improve strength, ductility and energy dissipation capacity of such walls. Masonry buildings can also be categorized as confined and unconfined. Using horizontal and/or vertical ties

✉ Ali Bakhshi
bakhshi@sharif.edu

Extended author information available on the last page of the article

Fig. 1 Example of damages to an Iranian URM school building in Ahar Earthquake, 2012; note that although the life safety performance level has been achieved, the servicability of the building halted temporarily. (Courtesy of Dr. Morteza Bastami)

usually in the form of lightly reinforced concrete members at the perimeter of walls, their intersection with perpendicular walls and if necessary, around large openings can considerably enhance their ductility and in some cases their strength.

Unlike other masonry construction types, the behavior of Confined unreinforced Masonry (referred to CM hereafter) buildings has not yet been fully formulated. This is mainly because of more sophisticated behavioral characteristics of CM walls compared to unconfined Unreinforced Masonry (referred to URM hereafter) buildings. CM is the only masonry system that has been allowed practicing by the Iranian Code of Practice for Seismic Resistant Design of Buildings (Standard 2800, 2005) in seismic-prone areas. Consequently, considering the fact that more than 6% of five million rural houses in Iran (Rural Houses Specifications Count 2003) and more than 20% of 95,000 Iranian schools (Yekrangnia and Mahdizadeh 2009) are CM, proper design and evaluation of these buildings are urgent and important as well. The current approach of the majority of seismic design codes for CM buildings (including Standard 2800) is prescriptive in nature, and are intended to provide a life-safety level of protection when a design-level earthquake occurs. However, a code-designed building could withstand extensive damages from a design-level earthquake, and be out of service for an extended period of time. In some cases, the damage may be too expensive to repair, leaving demolition and reconstruction as the only option (FEMA-P-58, 2012). This is indeed a challenging situation for school buildings that their operational performance is needed both for students and for possible immediate sheltering after earthquakes (Fig. 1).

In this paper, seismic performance of a typical Iranian masonry school building is evaluated by using previously-developed simple spring models (Yekrangnia et al. 2017a, b). Fragility curves are derived based on large number of records for two sets of seismic actions; far-field and pulse-including near-field records. Vulnerability of the considered CM school buildings are compared with the corresponding URM school buildings. Finally, the results of the fragility curves are utilized in risk assessment of masonry school buildings in Tehran following a scenario-based approach. It should be noted that the results of this study are limited to single-story URM buildings (either unconfined or confined). In this study, the out-of-plane failure of walls was not considered. Observations from past earthquakes by the first author (Yekrangnia et al. 2017a, b) indicate that if wall-to-wall connections were constructed according to national building design codes, the out-of-plane failure of walls is unlikely to occur especially for the low height-to-thickness (slenderness) ratio of most

Iranian URM walls. The out-of-plane resistance of such walls is significantly improved thanks to the presence of confining ties in CM buildings. However, care must be taken in such statement as in-plane (IP) and out-of-plane (OP) interaction of URM/CM walls can finally result in huge capacity reduction both in in-plane and out-of-plane directions (Dolatshahi et al. 2014; Dolatshahi and Yekrangnia 2015).

The summary of the utilized procedure of risk assessment of masonry school buildings in this study is presented in Fig. 2. The procedure consists of several stages which forms different sections of this paper. These include assembling the building performance model, performing IDA, defining building and performance characteristics, and calculating performance that together with defining earthquake hazards, leads to final results of seismic risk analysis. These steps will be fully covered in the following sections.

2 Assembling building performance models

2.1 Modeling procedure and assumptions

Modeling of walls in the CM school building was carried out by using the proposed models by Yekrangnia et al. (2017a, b) for CM walls. The force–displacement behavior found in ASCE 41 (ASCE 41–13, 2013) was utilized for modeling the corresponding URM school building. For this purpose, lateral drift ratio was considered for Engineering
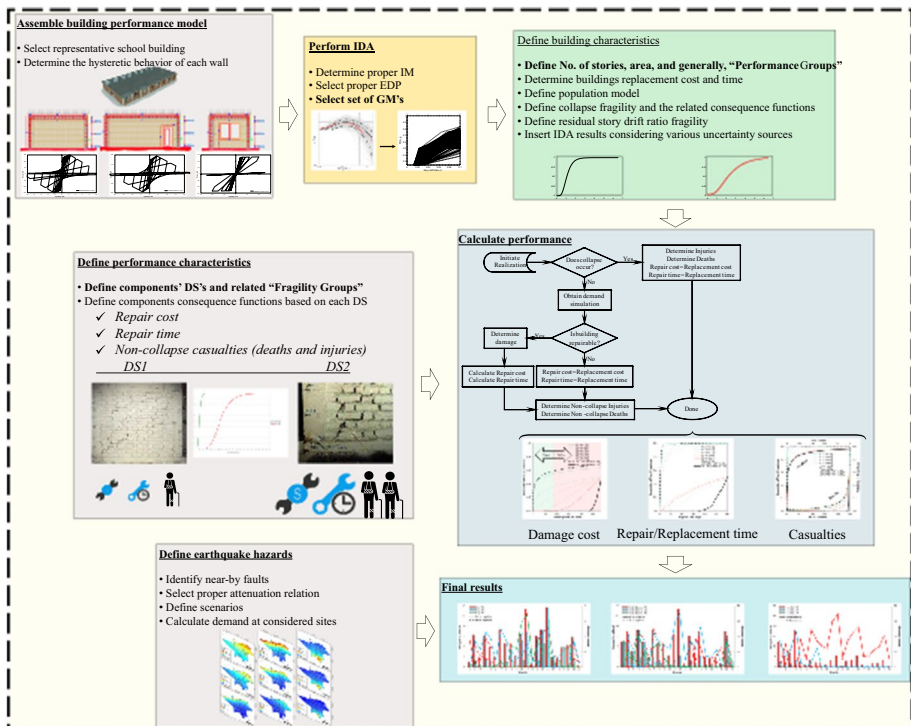

Fig. 2 Flowchart of risk assessment of masonry school buildings based on FEMA P-58 Methodology

Fig. 3 Utilized hysteretic behavior for solid and perforated CM walls (Yekrangnia et al. 2017a, b)
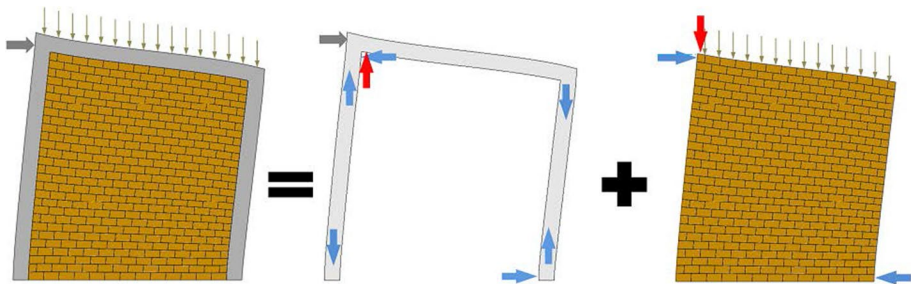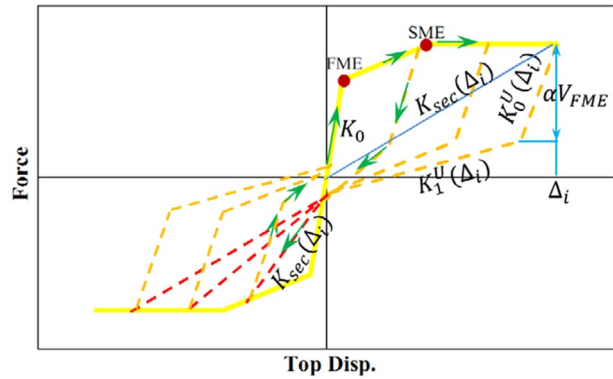

Fig. 4 Induced forces in wall and ties

Demand Parameter (EDP), as a parameter which best describes seismic response severity of each structural element (which can be drifts, accelerations, distortions, etc.) and was subsequently used to determine performance based on the proposed damage index (FEMA 440, 2005). Two levels of EDP's for drift ratios, namely First Major Event (FME) related to the first considerable stiffness reduction and Second Major Event (SME) associated with the ultimate force capacity of each wall, were considered. These EDP's were determined based on the relations proposed by Yekrangnia et al. (2017a, b) for various CM walls and also ASCE 41 of the corresponding URM walls. The schematic representation of the utilized hysteretic force–displacement behavior for CM walls is shown in Fig. 3. The backbone curve of this behavior is characterized by two points i.e. FME and SME. Based on this proposed behavior, the characteristics of CM walls up to FME (wall's cracking) including wall's strength and stiffness are similar to those of the corresponding URM walls which can be determined based on the available relations in different seismic design codes e.g. ASCE 41 (ASCE 41–13, 2013). The strength related to SME is based on the positive effects of confining ties in the form of an additional vertical compressive force from the tie acting on the wall. This interaction force as the confining force on the wall is shown with a red arrow in Fig. 4 which directly contributes to increasing the wall's shear-sliding capacity. The SME strength as the maximum strength of CM wall is the improved wall's capacity when either of the tensile, compressive or shear failure occurs in the ties; all of which can be determined based on available design code's formulations for reinforced concrete members. The displacement related to SME (Δ_{SME}) is based on equating

the previously-determined SME strength and the strength following the bilinear force–displacement path (as a function of unknown Δ_{SME}). The stiffness in the second branch of force–displacement curve (from FME to SME according to Fig. 3) is the reduced stiffness based on the experienced damages in the wall and the ties. In displacements larger than that of SME, the wall experiences strength softening if the failure of the ties is either compressive or shear. The loading mechanism follows a secant stiffness($K_{sec}(\Delta_i)$) based on the displacement demand (Δ_i).The unloading behavior follows a bilinear path through two stiffness factors i.e.$K_0^U(\Delta_i)$ and $K_1^U(\Delta_i)$ shown in Fig. 3. The former and the latter stiffness are functions of wall's initial stiffness and ties flexural stiffness, respectively. It is assumed that $K_0^U(\Delta_i)$ and $K_1^U(\Delta_i)$ linearly decrease by the displacement demand. The effects of opening are taken into account in the form CM wall's initial stiffness, the strength related to FME and SME; and also two reduction factors. The first reduction factor shown by α in Fig. 3 is applied to the unloading strength (V_{FME}) and the other is applied to $K_1^U(\Delta_i)$; both of which depend on the ratio of opening's length to that of the wall. More information about the proposed model is found in Yekrangnia et al. (2017a, b).

2.2 Considered failure modes for CM and URM walls

Generally speaking, among the possible failure modes in CM walls, shear-sliding in walls and three failure modes in ties namely shear failure at the base of the Far Tie (FT), tensile failure at the base of the Near Tie (NT) and compression failure at the base of the FT have been observed in Iranian CM walls. Schematic representation of these failure modes are shown in Fig. 5. It can be said that for walls with low aspect ratios (the ratio of height to length of the wall), shear failure in ties is more probable (Yekrangnia et al. 2017a, b). For walls having high aspect ratios and a considerable vertical load, compression failure at the ties is more likely; and for walls with an intermediate aspect ratio, the ties' tensile failure is expected. Each of the aforementioned failure modes of CM walls has its own characteristics in terms of the force–displacement curve and hysteretic behavior. The detailed
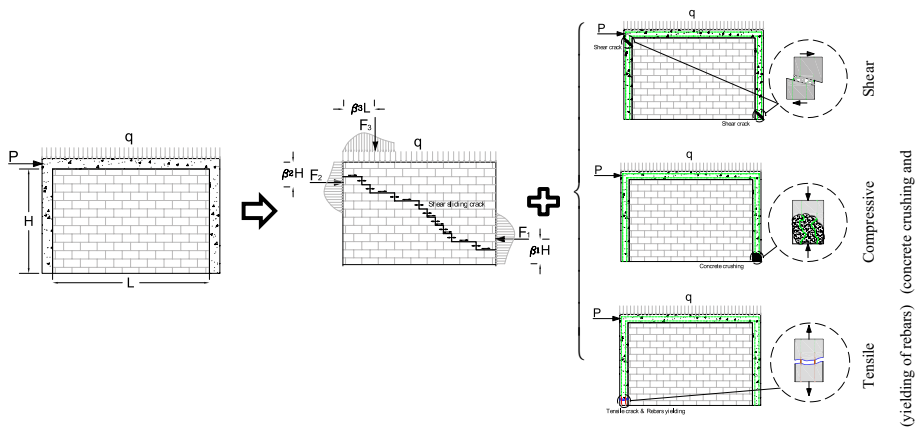

Fig. 5 Considered failure modes in wall and ties in CM walls **a** After Tasnimi (2004) (Failure mode: shear sliding in wall/tensile failure in tie) **b** After KhalafRezaei (2012) (Failure mode: shear sliding in wall/compressive failure in tie) **c** After Sarrafi and Eshghi (2012) (Failure mode: shear sliding in wall/tensile failure in tie)

formulations for determination of the parameters related to force–displacement behavior of CM walls are found in Yekrangnia et al. (2017a, b).

In order to further verify the accuracy of the proposed formulations in capturing the hysteretic behavior of CM walls, the results of three previously-tested specimens are exploited. The characteristics of these specimens are found in Table 1. In this table, *H*, *L* and *t* are wall's height, length, and thickness, respectively; *b* and *d* are the width and height of ties' cross section, respectively; μ is the friction coefficient between bricks; f'_m and f'_c are compressive strengths of masonry prism and concrete of ties, respectively; f_y is the yield strength of longitudinal bars in ties which is equal to yield strength of shear reinforcement in ties (f_{y-tie}); *q* and *C* are vertical stress on the wall and shear bond strength of mortar, respectively; d_{tie} and d_{rebar} are the diameter of shear and longitudinal reinforcing bars in ties, respectively; *s* is the distance between shear reinforcement bars; Δ_{FME} and Δ_{SME} are lateral drift ratios related to FME and SME, respectively.

The numerical simulation of the specimens is performed using OpenSees (Fenves et al. 2004). For this purpose, the required parameters derived from the proposed relations by Yekrangnia et al. (2017a, b) are assigned to Pinching4 material in a single degree of freedom system as a nonlinear axial spring. Where as shown in Fig. 6, shear stress-lateral drift ratio curves of the experimental specimens and the numerical models are in good agreement which indicates the ability of the models to simulate different behavioral characteristics of CM walls. The force–displacement curves of the models and related specimens have been transformed to shear stress-lateral drift ratio in order to make them independent of the walls' geometrical characteristics. Part (a) and (b) of this figure represent solid CM walls with sliding shear failure in the wall but with different failure modes in the ties. The specimen in part (a) experiences tensile failure in the NT which is associated with a large displacement capacity up to 3% of drift ratio as shown in this figure; whereas in part (b), compressive failure occurs in the FT which is attributed to significant strength reduction in larger drift ratios. The considered specimen in part (c) of this figure has a central window with 0.60 m and 0.45 m in length and height, respectively. The wall and the NT experience shear sliding and tensile failure, respectively. The noticeable pinching in the hysteretic curve in this specimen compared to the two others originates from presence of opening which results in considerable reduction of the wall's stiffness. As a result, ties play a more important role in load-bearing mechanism and the behavior of this specimen tends to that in a typical infilled frame with weak infill/strong frame which in many cases shows pinching (Yekrangnia and Mohammadi 2017).

2.3 Models selection

The main objective of this study is to derive analytical-based fragility curves for masonry buildings. For this purpose, a representative Iranian masonry school building shown in Fig. 7 is considered. The dimensions of different parts of the representative school building are based on the mean values from statistical analysis on more than 500 masonry school buildings in Iran by the first author (Yekrangnia et al. 2017a, b). Unfortunately, among the related mechanical properties of material, only shear strength of mortar is available from several in-situ tests (see Fig. 8) and the median value of this parameter has been considered for performing IDA. Selection of this value is based on FEMA-P-58 (FEMA-P-58 2012) recommendation which indicates the 50th percentile values are appropriate for estimating quantities for most buildings, when more specific information is not available about buildings under consideration. In addition to shear strength of mortar, other material properties

Table 1 Characteristics of the benchmark tests specimens

| Specimen	H (m)	L (m)	t (m)	μ	q (MPa)	C (MPa)	fm' (MPa)	f_c' (MPa)	f_y (MPa)	b (m)	d (m)	d_{tie} (mm)	d_{rebar} (mm)	s (m)	Δ_{FME} (%)	Δ_{SME} (%)
CBW2[1]	2.0	2.6	0.22	0.53	0.15	0.21	8.5	27.7	333	0.20	0.17	4	8	0.13	0.11	2.88
CM-S[2]	2.6	2.6	0.20	*0.75**	0.02	0.50	7.9	12.5	353	0.20	0.18	8	12	0.15	0.01	0.23
CMOW-01[3]	1.5	2.2	0.11	*0.50**	0.09	0.18	1.7	19.6	*240**	0.10	*0.08**	4	6	0.08	0.19	0.36

*The parameters in italic were not found explicitly in the related reference. They have been derived based on the available similar data. [1](Tasnimi 2004); [2](KhalafRezaei 2012); [3](Sarrafi and Eshghi 2012)
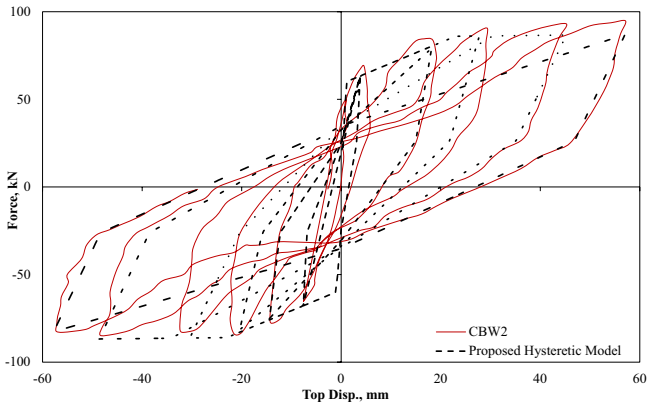
(a) After Tasnimi, 2004 (Failure mode: shear sliding in wall/tensile failure in tie)
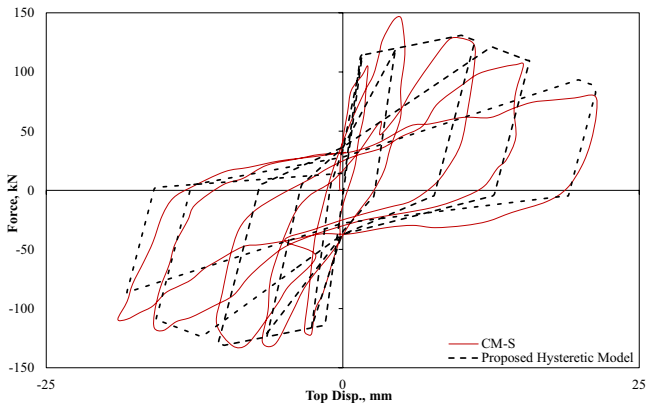
(b) After KhalafRezaei, 2012 (Failure mode: shear sliding in wall/compressive failure in tie)
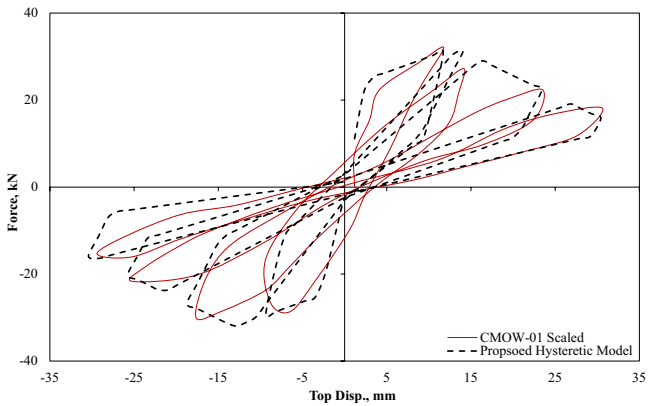
(c) After Sarrafi and Eshghi, 2012 (Failure mode: shear sliding in wall/tensile failure in tie)

Fig. 6 Comparison of force–displacement curves of the experimental specimens and the proposed numerical models after Yekrangnia et al. (2017a, b)

Fig. 7 Representative Iranian CM school building (Assumed values: c = 0.22 MPa, f'_c = 20MPa, f'_m = 3MPa, f_{y-tie} = 240MPa, f_y = 400MPa, Roof mass = 820 $\frac{kg}{m^2}$)
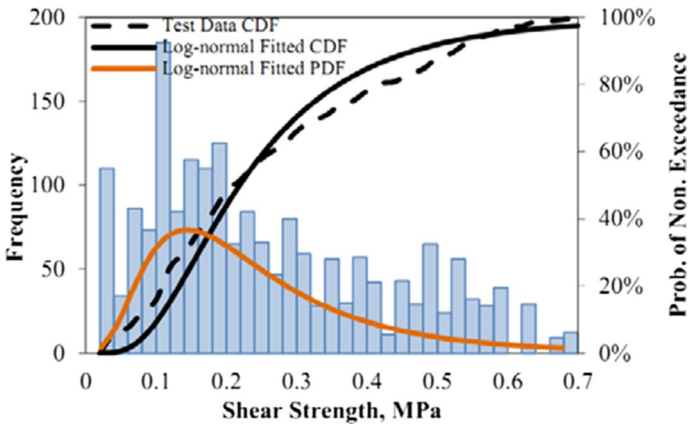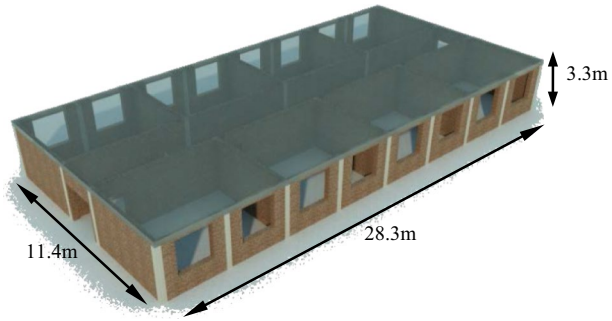

Fig. 8 Distribution of mortar shear strength by in-situ tests on 1914 samples based on EN 1052-3 (2002); with mean and standard deviation of 0.26 MPa and 0.17 MPa, respectively

such as compressive strength of concrete, yield strength of bars, and compressive strength of masonry prism are necessary for developing spring models. These parameters were assumed based on the values found in Tasnimi (2004).

It is worth noting that because many Iranian masonry school buildings are symmetrical in both directions and the geometrical characteristics of all classrooms are similar, they are considered as modular buildings and hence the number of classrooms has negligible effects on their seismic performance. Because of the modularity of classrooms, the connections of the adjacent walls at each building plan axis is not much of importance. For example, consider a single classroom with two parallel walls in each direction, if the initial stiffness and strength capacity of such walls in direction 1 can be represented by parameters K, and F, respectively, these parameters for double-classroom building is approximately 2 K and 2F, respectively (Mosalam et al. 1997). The mass of the latter building is two times of that of the former building. Consequently, the seismic demands on the two buildings are approximately identical and the capacity of each module (classroom) remains approximately constant regardless of the number of classrooms. Consequently, the fragility curve for the representative classroom can be regarded very similar to that of the whole building. Consequently, seismic behavior of Iranian masonry school buildings can be represented by the behavior a representative classroom consisting of

several modular walls in both directions. These walls are schematically shown in Fig. 9 with their behavior in terms of shear stress-lateral drift ratio at the second row. The ratio of opening to the walls' surface area for walls with door and window is 10%, and 22%, respectively. It is noted that based on some design recommendations (Meli et al. 2011), this ratio is limited to a certain upper bound. However, the aim of this study is to perform seismic risk analysis on a typical URM and corresponding CM representative building regardless of the consideration of seismic design code's requirements. The dashed lines in these curves represent shear stress-lateral drift ratio of the considered URM walls according to ASCE 41 (ASCE 41–13, 2013). The solid lines signify the behavior of the corresponding CM walls based on Yekrangnia et al. (2017a, b). Since the failure mode of all the URM walls are rocking, zero hysteretic damping is considered for these walls and hence, the unloading behavior exactly follows the loading curve in these diagrams. As a result, both dashed and solid lines denote cyclic behavior of the considered walls. As shown in Fig. 9, NS-S is a solid wall in North–South direction (two of them are considered in a parallel spring model later in obtaining fragility curves for the representative classroom); EW-D and EW-W are the walls with side door and central window in the East–West direction (see Fig. 7), respectively. Note that in each representative classroom, there are two identical EW-W walls which are adjacent to each other and the response of two EW-W walls is included for determination of the representative classroom's vulnerability. Because of a common-practice system of jack-arch roof in which the roof's beams are placed on the walls in EW direction, NS-S is assumed to be non-load-bearing in the vertical direction; whereas the roof loads of each classroom are equally distributed between EW-D and two EW-W walls. Moreover, EW-D bears the roof load from the corridor of the building. Among the behavioral characteristics of these walls is considerable reduction in hysteretic damping of EW-W due to presence of large opening ratio (ratio of opening area to wall area). Also, EW-W has larger displacement capacity compared to NS-S and EW-D because of the lower wall's contribution in load-bearing originated from significantly lower stiffness compared with other walls. However in NS-S and EW-D, the wall dominates the lateral response because of its length and therefore, the resulted stiffness and shear strength. As a result, these walls have less displacement capacity because of inherent limited-ductility nature
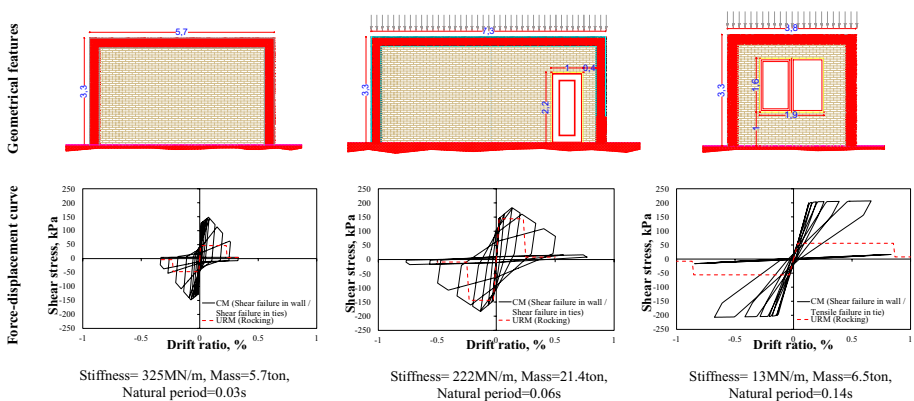

Fig. 9 Geometrical features and force–displacement of the CM walls and the corresponding URM walls in the representative building (dimensions in m) **a** Far-field set **b** Near-field set

of masonry walls. It is noted that the walls were assumed to carry in-plane loads only and no out-of-plane contribution was considered for the walls.

By comparing the shear stress-lateral drift ratio behavior of the considered URM walls with that of the corresponding CM walls, it is observed that significant improvement is achieved thanks to the confining effects from the ties especially in NS-S and EW-W. As shown by Yekrangnia et al. (2017a, b), masonry walls benefit most from the confining elements in in two cases: (1) the vertical loads are negligible; which usually means the failure mode changes from rocking in URM wall to diagonal-sliding in the corresponding CM wall due to confining force from the tie (shown in Fig. 4); or (2) the wall's aspect ratio is high which intensifies the confining force from the tie. Case (1) and case (2) are valid for NS-S and EW-W, respectively; the former bears no vertical force from the roof and the latter is divided by the central window into two separate piers with a high aspect ratio. It is noted that for NS-S and EW-D, the capacity related to shear failure and tensile failure at the ties are close to each other. For these walls, the shear failure at the ties which is attributed to less ductility is considered conservatively. On the other hand, for all the URM walls, the toe-crushing and rocking failure modes are close matches. For these walls, the ductile rocking failure mode is considered un-conservatively to compare the positive effects of confining ties in the worst case possible.

3 Performing IDA

3.1 Records characteristics

In this part, characteristics of the earthquake records used for performing IDA are presented. Two sets of records namely far-field and near-field are considered in this paper. Based on Benjamin and Cornell (1970), the number of required ground motions for performing IDA is determined based on the standard deviation of EDP's and the assumed error. In this study, the number of considered earthquakes is sufficient to maintain a maximum error of 2% in the results.

3.1.1 Far-field records

The far-field set consists of 60 records which covers soil classes B, C and D based on ASCE 41–13, 2013. These records are recommended as the far-field records by FEMA P-440A (2009). This set is employed in this study as an indicator for determination of sensitivity of the considered walls to the near-field ground motions. The acceleration spectrum of this set scaled to the design Peak Ground Acceleration (PGA) in conjunction with the average of the design spectrum of Standard 2800, 2005 over the soil classes B, C and D for regions with very high seismicity has been shown in Fig. 10a. Also, the list of the far-field records used in this study is found in Table 2.

3.1.2 Near-field records

The near-field set, including 266 pulse-like ground motions recorded on soil classes B, C and D was downloaded from PEER strong motion database (Chiou et al. 2008). Figure 10b shows the acceleration spectrum of this set scaled to the design PGA. As stated by Lovon et al. (2018), considering a large set of ground motion records provides good
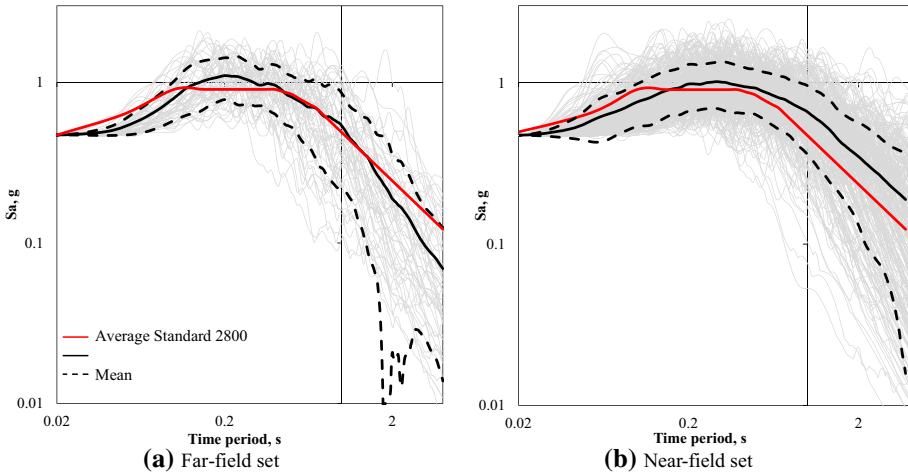
Fig. 10 Acceleration response spectra of the considered ground motions

propagation of the record-to-record variability. Comparing the spectra of the far-field set and the near-field set in this figure shows higher spectral accelerations at large periods in the latter set that was addressed in several previous studies (Ghahari et al. 2010). Also, the list of the near-field records used in this study is presented in Table 3. As indicated in design codes (ASCE/SEI 7–05 2005), the selected ground motions should represent the magnitude, fault-to-site distance and fault mechanism of the seismic actions in the considered site. Since the final objective of this study is to evaluate the risk of masonry school buildings in the city of Tehran which is surrounded by three major faults (two of which are less than 10 km distance from the city), considering the near-field, pulse-like earthquakes in developing fragility curves can greatly facilitate a deeper understanding of a more realistic performance of these buildings. Also, since these buildings have high natural frequencies, they are expected to show sensitivities to high-frequency content related to near-field ground motions.

According to the findings by Bommer et al. (2004) on the effect of duration of ground motions on masonry buildings with strength and stiffness degradation, some of the records which caused higher strength degradation in masonry buildings are from events with pulse-like, near-field ground motions. Also, he concluded that near-field records which impose considerable energy on the structures in a short period of time tend to cause severer damages compared to far-field ground motions with the same energy which is distributed over a longer period of time. This observation has also been pointed out by FEMA 461 (2007). However, Kostov and Koela (2007) stated that although near-field ground motions has high PGA's, they result in lighter damages compared to far-field earthquakes which usually have significant Cumulative Absolute Velocities (CAV). These rather diverse findings make the evaluation of the effects of near-field earthquakes on performance of the considered masonry buildings more interesting.

3.2 Strong motion parameters

In this study, several strong motion parameters are considered as intensity measures to correlate with the selected EDP i.e. maximum drift ratio. As reported by Bakhshi et al. (2014),

Table 2 Characteristics of far-field ground motions in this study

No.	Event	Year	Station name	Mechanism	Site class	No.	Event	Year	Station name	Mechanism	Site class
1	Landers	1992	Silent valley—poppet flat	Strike slip	B	31	Loma prieta	1989	Fremont—mission san jose	Reverse oblique	C
2	Landers	1992	Twentynine palms	Strike slip	B	32	Loma prieta	1989	Monterey city hall	Reverse oblique	C
3	Landers	1992	Amboy	Strike slip	B	33	Loma prieta	1989	Yerba buena island	Reverse oblique	C
4	Loma prieta	1989	Point bonita	Reverse oblique	B	34	Loma prieta	1989	Anderson dam (downstream)	Reverse oblique	C
5	Loma prieta	1989	Piedmont Jr high school grounds	Reverse oblique	B	35	Morgan hill	1984	Gilroy—gavilan coll	Strike slip	C
6	Loma prieta	1989	SF—pacific heights	Reverse oblique	B	36	Morgan hill	1984	Gilroy array #6	strike slip	C
7	Loma prieta	1989	SF—rincon hill	Reverse oblique	B	37	N. Palm springs	1986	Fun valley	Reverse oblique	C
8	Loma prieta	1989	Golden gate bridge	Reverse oblique	B	38	Northridge-01	1994	Littlerock—brainard can	Reverse	C
9	Loma prieta	1989	Hollister—SAGO Vault	Reverse oblique	B	39	Northridge-01	1994	Castaic—old ridge route	Reverse	C
10	Loma prieta	1989	So. San francisco, Sierra Pt	Reverse oblique	B	40	Northridge-01	1994	Lake hughes #1	Reverse	C
11	Loma prieta	1989	Berkeley LBL	Reverse oblique	B	41	Landers	1992	Yermo fire station	Strike Slip	D
12	Loma prieta	1989	Coyote lake dam (Downst)	Reverse oblique	B	42	Landers	1992	Palm springs airport	Strike slip	D
13	Northridge-01	1994	Mt Wilson—CIT Seis Sta	Reverse	B	43	Landers	1992	Pomona—4th and locust FF	Strike slip	D
14	Northridge-01	1994	Antelope buttes	Reverse	B	44	Northridge-01	1994	LA—hollywood stor FF	Reverse	D
15	Northridge-01	1994	LA—Wonderland Ave	Reverse	B	45	Northridge-01	1994	Santa monica city hall	Reverse	D
16	Northridge-01	1994	Wrightwood—jackson flat	Reverse	B	46	Northridge-01	1994	LA—N westmoreland	Reverse	D
17	Northridge-01	1994	Littlerock—brainard can	Reverse	B	47	Loma prieta	1989	Gilroy array #2	Reverse oblique	D

Table 2 (continued)

No.	Event	Year	Station name	Mechanism	Site class	No.	Event	Year	Station name	Mechanism	Site class
18	Northridge-01	1994	San Gabriel—E grand ave	Reverse	B	48	Loma Prieta	1989	Gilroy array #3	Reverse oblique	D
19	Whittier narrows-01	1987	LA—baldwin hills	Reverse oblique	B	49	Loma prieta	1989	APEEL 2E hayward muir sch	Reverse oblique	D
20	Imperial Valley-06	1979	Superstition mtn camera	Strike slip	B	50	Loma prieta	1989	Agnews State Hospital	Reverse oblique	D
21	Imperial valley-06	1979	Parachute test site	Strike slip	C	51	Whittier narrows-01	1987	LA—116th St school	Reverse oblique	D
22	San fernando	1971	Pasadena—CIT athenaeum	Reverse	C	52	Whittier narrows-01	1987	Downey—Co maint bldg	Reverse oblique	D
23	San fernando	1971	Pearblossom pump	Reverse	C	53	Imperial valley-06	1979	El Centro array #13	Strike slip	D
24	Landers	1992	Yermo fire station	Strike slip	C	54	Imperial valley-06	1979	Calexico fire station	Strike slip	D
25	Loma prieta	1989	APEEL 7—pulgas	Reverse oblique	C	55	Morgan hill	1984	Gilroy array #2	Strike slip	D
26	Loma prieta	1989	Gilroy Array #6	Reverse oblique	C	56	Morgan hill	1984	Gilroy array #3	Strike slip	D
27	Loma prieta	1989	Saratoga—aloha ave	Reverse oblique	C	57	Morgan hill	1984	Gilroy array #4	Strike slip	D
28	Loma prieta	1989	Gilroy—gavilan coll	Reverse oblique	C	58	Morgan hill	1984	Gilroy array #7	Strike slip	D
29	Loma prieta	1989	UCSC	Reverse oblique	C	59	San fernando	1971	LA—hollywood stor FF	Reverse	D
30	Loma prieta	1989	SF—diamond heights	Reverse oblique	C	60	San fernando	1971	LB—terminal island	Reverse	D

Table 3 Characteristics of near-field ground motions in this study

No.	Event	Year	Station name	Mechanism	Site class	No.	Event	Year	Station name	Mechanism	Site class
1	Tabas, Iran	1978	Tabas	Reverse	B	67	Niigata, Japan	2004	NIG021	Reverse	C
2	Landers	1992	Lucerne	Strike slip	B	68	Niigata, Japan	2004	NIGH11	Reverse	C
3	Kocaeli, Turkey	1999	Gebze	Strike slip	B	69	Montenegro, Yugoslavia	1979	Bar-Skupstina opstine	Reverse	C
4	Kocaeli, Turkey	1999	Izmit	Strike slip	B	70	L'Aquila, Italy	2009	L'Aquila—V. Aterno—centro valle	Normal	C
5	Loma Prieta	1989	Los Gatos—lexington dam	Reverse oblique	B	71	L'Aquila, Italy	2009	L'Aquila—V. Aterno -F. Aterno	Normal	C
6	Coyote Lake	1979	Gilroy array #6	Strike slip	C	72	L'Aquila, Italy	2009	L'Aquila—parking	Normal	C
7	Irpinia, Italy-01	1980	Bagnoli irpinio	Normal	C	73	Chuetsu-oki, Japan	2007	Joetsu kakizakiku kakizaki	Reverse	C
8	Irpinia, Italy-01	1980	Sturno (STN)	Normal	C	74	Darfield, New Zealand	2010	LPCC	Strike slip	C
9	Morgan hill	1984	Coyote lake dam—Southwest	Strike Slip	C	75	Duzce, Turkey	1999	IRIGM 487	Strike slip	C
10	Morgan hill	1984	Gilroy array #6	Strike Slip	C	76	Coyote lake	1979	Gilroy array #2	Strike slip	D
11	Kalamata, Greece-02	1986	Kalamata (bsmt) (2nd trigger)	Normal	C	77	Coyote lake	1979	Gilroy array #3	Strike slip	D
12	San Salvador	1986	Geotech Investig Center	Strike slip	C	78	Coyote lake	1979	Gilroy array #4	Strike Slip	D
13	San Salvador	1986	National Geografical Inst	Strike slip	C	79	Imperial valley-0	1979	Agrarias	Strike slip	D
14	Loma Prieta	1989	Saratoga—Aloha Ave	Reverse oblique	C	80	Imperial valley-06	1979	Brawley airport	Strike slip	D
15	Cape Mendocino	1992	Petrolia	Reverse	C	81	Imperial valley-06	1979	EC County center FF	Strike slip	D
16	Landers	1992	Barstow	Strike slip	C	82	Imperial valley-06	1979	El Centro—Meloland geot. array	Strike slip	D

Table 3 (continued)

No.	Event	Year	Station name	Mechanism	Site class	No.	Event	Year	Station name	Mechanism	Site class
17	Northridge-01	1994	Jensen filter plant administrative	Reverse	C	83	Imperial valley-06	1979	El Centro array #10	Strike slip	D
18	Northridge-01	1994	Jensen filter plant generator building	Reverse	C	84	Imperial valley-06	1979	El Centro array #4	Strike slip	D
19	Northridge-01	1994	LA—sepulveda VA hospital	Reverse	C	85	Imperial valley-06	1979	El Centro array #5	Strike slip	D
20	Northridge-01	1994	LA dam	Reverse	C	86	Imperial valley-06	1979	El Centro array #6	Strike slip	D
21	Northridge-01	1994	Pacoima kagel canyon	Reverse	C	87	Imperial valley-06	1979	El Centro array #7	Strike slip	D
22	Northridge-01	1994	Sylmar—converter sta east	Reverse	C	88	Imperial valley-06	1979	El Centro differential array	Strike Slip	D
23	Northridge-01	1994	Sylmar—olive view med FF	Reverse	C	89	Imperial valley-06	1979	Holtville post office	Strike slip	D
24	Kocaeli, Turkey	1999	Arcelik	Strike slip	C	90	Westmorland	1981	Parachute test site	Strike slip	D
25	Chi-Chi, Taiwan	1999	CHY006	Reverse oblique	C	91	Superstition hills-02	1987	Kornbloom road (temp)	Strike slip	D
26	Chi-Chi, Taiwan	1999	CHY024	Reverse oblique	C	92	Superstition hills-02	1987	Parachute test site	Strike slip	D
27	Chi-Chi, Taiwan	1999	NST	Reverse oblique	C	93	Loma prieta	1989	Gilroy—Historic Bldg	Reverse oblique	D
28	Chi-Chi, Taiwan	1999	TCU026	Reverse oblique	C	94	Loma prieta	1989	Gilroy array #2	Reverse oblique	D
29	Chi-Chi, Taiwan	1999	TCU029	Reverse oblique	C	95	Loma prieta	1989	Gilroy array #3	Reverse oblique	D
30	Chi-Chi, Taiwan	1999	TCU031	Reverse oblique	C	96	Loma prieta	1989	Saratoga—W valley coll	Reverse oblique	D
31	Chi-Chi, Taiwan	1999	TCU033	Reverse oblique	C	97	Landers	1992	Yermo fire station	Strike slip	D
32	Chi-Chi, Taiwan	1999	TCU034	Reverse oblique	C	98	Northridge-01	1994	Newhall—fire sta	Reverse	D
33	Chi-Chi, Taiwan	1999	TCU036	Reverse oblique	C	99	Northridge-01	1994	Newhall—W pico canyon Rd	Reverse	D

Table 3 (continued)

No.	Event	Year	Station name	Mechanism	Site class	No.	Event	Year	Station name	Mechanism	Site class
34	Chi-Chi, Taiwan	1999	TCU039	Reverse oblique	C	100	Northridge-01	1994	Pardee—SCE	Reverse	D
35	Chi-Chi, Taiwan	1999	TCU040	Reverse oblique	C	101	Northridge-01	1994	Rinaldi receiving Sta	Reverse	D
36	Chi-Chi, Taiwan	1999	TCU045	Reverse oblique	C	102	Northridge-01	1994	Sylmar—converter Sta	Reverse	D
37	Chi-Chi, Taiwan	1999	TCU046	Reverse oblique	C	103	Kobe, Japan	1995	KJMA	Strike slip	D
38	Chi-Chi, Taiwan	1999	TCU047	Reverse oblique	C	104	Kobe, Japan	1995	Port Island (0 m)	Strike slip	D
39	Chi-Chi, Taiwan	1999	TCU049	Reverse oblique	C	105	Kobe, Japan	1995	Takarazuka	Strike slip	D
40	Chi-Chi, Taiwan	1999	TCU052	Reverse oblique	C	106	Kobe, Japan	1995	Takatori	Strike slip	D
41	Chi-Chi, Taiwan	1999	TCU053	Reverse oblique	C	107	Kocaeli, Turkey	1999	Yarimca	Strike slip	D
42	Chi-Chi, Taiwan	1999	TCU056	Reverse oblique	C	108	Chi-Chi, Taiwan	1999	CHY101	Reverse oblique	D
43	Chi-Chi, Taiwan	1999	TCU063	Reverse oblique	C	109	Chi-Chi, Taiwan	1999	TCU038	Reverse oblique	D
44	Chi-Chi, Taiwan	1999	TCU064	Reverse oblique	C	110	Chi-Chi, Taiwan	1999	TCU051	Reverse oblique	D
45	Chi-Chi, Taiwan	1999	TCU068	Reverse oblique	C	111	Chi-Chi, Taiwan	1999	TCU059	Reverse oblique	D
46	Chi-Chi, Taiwan	1999	TCU075	Reverse oblique	C	112	Chi-Chi, Taiwan	1999	TCU065	Reverse oblique	D
47	Chi-Chi, Taiwan	1999	TCU076	Reverse oblique	C	113	Duzce, Turkey	1999	Bolu	Strike slip	D
48	Chi-Chi, Taiwan	1999	TCU082	Reverse oblique	C	114	Denali, Alaska	2002	TAPS Pump Station #10	Strike slip	D
49	Chi-Chi, Taiwan	1999	TCU087	Reverse oblique	C	115	Parkfield-02, CA	2004	Parkfield—Cholame 1E	Strike slip	D
50	Chi-Chi, Taiwan	1999	TCU101	Reverse oblique	C	116	Parkfield-02, CA	2004	Parkfield—Cholame 3 W	Strike slip	D
51	Chi-Chi, Taiwan	1999	TCU102	Reverse oblique	C	117	Parkfield-02, CA	2004	Parkfield—Fault Zone 12	Strike slip	D
52	Chi-Chi, Taiwan	1999	TCU103	Reverse oblique	C	118	Parkfield-02, CA	2004	Parkfield—Stone Corral 1E	Strike slip	D
53	Chi-Chi, Taiwan	1999	TCU104	Reverse oblique	C	119	Montenegro, Yugoslavia	1979	Ulcinj—Hotel Olimpic	Reverse	D

Table 3 (continued)

No.	Event	Year	Station name	Mechanism	Site class
54	Chi-Chi, Taiwan	1999	TCU128	Reverse oblique	C

Table 3 (Continued) Characteristics of near-field ground motions in this study

No.	Event	Year	Station name	Mechanism	Site class
55	Chi-Chi, Taiwan	1999	TCU136	Reverse oblique	C
56	Chi-Chi, Taiwan-04	1999	CHY074	Strike Slip	C
57	Chi-Chi, Taiwan-06	1999	TCU078	Reverse	C
58	Chi-Chi, Taiwan-06	1999	TCU080	Reverse	C
59	Cape Mendocino	1992	Bunker Hill FAA	Reverse	C
60	Cape Mendocino	1992	Centerville Beach, Naval Fac	Reverse	C
61	Bam, Iran	2003	Bam	Strike slip	C
62	Parkfield-02, CA	2004	Parkfield—eades	Strike slip	C
63	Parkfield-02, CA	2004	Slack Canyon	Strike slip	C
64	Parkfield-02, CA	2004	Parkfield—cholame 3E	Strike slip	C
65	Parkfield-02, CA	2004	Parkfield—cholame 4 W	Strike slip	C
66	Parkfield-02, CA	2004	Parkfield—fault zone 9	Strike slip	C

No.	Event	Year	Station name	Mechanism	Site class
120	Darfield, New Zealand	2010	Christchurch Botanical Gardens	Strike slip	D
121	Darfield, New Zealand	2010	DSLC	Strike slip	D
122	Darfield, New Zealand	2010	GDLC	Strike slip	D
123	Darfield, New Zealand	2010	HORC	Strike slip	D
124	Darfield, New Zealand	2010	LINC	Strike slip	D
125	Darfield, New Zealand	2010	NNBS North New Brighton school	Strike slip	D
126	Darfield, New Zealand	2010	Riccarton high school	Strike slip	D
127	Darfield, New Zealand	2010	ROLC	Strike slip	D
128	Darfield, New Zealand	2010	Shirley library	Strike slip	D
129	Darfield, New Zealand	2010	Styx mill transfer station	Strike slip	D
130	Darfield, New Zealand	2010	TPLC	Strike slip	D
131	Christchurch, New Zealand	2011	Pages road pumping station	Reverse oblique	D
132	El Mayor-Cucapah, Mexico	2010	El Centro array #12	Strike slip	D
133	El Mayor-Cucapah, Mexico	2010	Westside elementary school	strike slip	D

the Park-Ang damage index for CM walls is best correlated with Effective Peak Acceleration (EPA), Arias Intensity (I_a), spectral acceleration at the first natural period ($S_d(T_1)$) and PGA. However, according to the study by Amiri and Dana (2005) in which they investigated sensitivity of several strong motion features of 150 Iranian earthquakes, EPA, Peak Ground Velocity (PGV) and Effective Peak Velocity (EPV) are the more prominent strong motion parameters for selecting the critical ground motions similar to one introduced by Zhai and Xie (2007). They concluded that velocity-related parameters are more representative of criticality of ground motions than displacement parameters which their sensitivity to low-frequency, high-amplitude signals is not reliable. This finding agrees with the results by Bommer et al. (2004) who stated that the dependency of duration on structural damages is open for further research. It is because inherent difficulty in decoupling the duration from other features of strong motion and this characteristic is expected to be influential in structures with low-cycle fatigue and cyclic degradation only (Bommer et al. 2004; Reinoso et al. 2000). Also, definition of duration and the considered damage type is of great importance which sometimes can result in independence of this parameter to the EDP (Shome et al. 1998).

Moreover, the duration of ground motion which is comparatively high in far-field earthquakes is not much of importance is some of EDP's including those related to extreme (as opposed to cumulative) response characteristics. Examples of these EDP's are maximum acceleration, maximum story shear force and maximum drift ratio which is considered in this study. As indicated by Bommer et al. (2004), unlike DI's which are based on energy dissipation, those based on extreme drift ratio are not sensitive to duration of strong motion.

As utilized in some researches (FEMA-P-58 2012), spectral acceleration at the dominant natural period of the structure is a frequently-used parameter as Intensity Measure (IM). Nonetheless, studies show that this parameter can results in high dispersions in EDP (Bommer et al. 2004). On the other hand, averaging the spectral accelerations over a range of periods is suggested. Since masonry buildings experience severe stiffness and sometimes strength reduction during earthquakes, the upper-bound of periods is very important in scaling the ground motions. While different codes consider different upper-bounds for scaling (Standard 2800 2005; NZS1170.5 2004), Bommer et al. 2004 found the $2.7T_1$ leads to the least dispersion in the EDP for masonry buildings in which T_1 is the natural period of the first mode of the building. When compared to single period scaling method, this method leads to less dispersion in the results; however, this is not the case for low-period structures e.g. single-story masonry buildings in which acceleration-related parameters works better (Dhakal et al. 2007). In this study, the proper IM is selected based on the results of sensitivity analysis presented in the next section "Selection of intensity measure".

3.3 IDA results discussion

3.3.1 Selection of intensity measure

There are several studies with the focus of determining the most efficient and sufficient IM for performing IDA. Luco and Cornell (2007) carried out sensitivity analysis on different types structures to different IM's. They found that ground motion intensity measure which takes into account second-mode frequency content and inelasticity is suitable in estimating the structural drift response measure. They also indicated that using this IM, it is not necessary to treat near-field ground motions as a separate set with far-field one. Jalayer

et al. (2012) and Ebrahimian et al. (2015) proposed and implemented a new procedure employing relative sufficiency measure based on information theory concepts to quantify the suitability of one IM relative to another in the representation of ground motion uncertainty. They found that the results depend only on the spectral ordinates at the periods of the first two modes of vibration. In order to determine the best parameter for IM for incrementally scaling the records sets for performing IDA and accordingly, deriving the fragility curves, a preliminary IDA is performed. Based on the results of this analysis which is not presented here for brevity, the correlation between the considered EDP i.e. the maximum story drift ratio and different strong motion parameters is studied. Among different strong motion parameters, PGA has the best correlation with the considered EDP i.e. maximum drift ratio. Consequently, PGA is considered here as IM. This correlation for two of the considered walls against two sets of the used ground motions is shown in Fig. 11. In this figure, the two sets of considered records namely near-field and far-field are applied incrementally to the two representative walls (NS-S and EW-W). Scale 1 in the legends of this figure means all the records are applied without any scaling and hence, in the intensity perspective, they are as-occurred earthquakes. Scale 2 records are scaled up two times of their original intensity. The other levels of applied excitation follow the same procedure with Scale i denoting the scale factor equal to i-times of the original records. As can be seen, since the near-field set has higher original intensity compared to the far-field set, lower scaling factors are needed to impose a very large EDP and hence complete the IDA process. According to Fig. 11, the similarities of the correlation between the IM and the EDP to the assumed force–displacement curve of the walls (placed at the top right within each figure for that particular wall) up to the SME level is observable. Also, the aforementioned correlation is weaker in EW-W compared to NS-S because this wall has a lower natural frequency (refer to Fig. 9) and hence, has lower sensitivity to acceleration-related strong motion parameters e.g. PGA. Two levels of drift ratio i.e. Δ_{FME} and Δ_{SME} associated with FME and SME, respectively which are based on the proposed relations by Yekrangnia et al. (2017a, b) are shown by vertical dashed lines. As can be seen, for the experienced drift ratios smaller than D_{FME}, the correlation is very strong which is due to the fact that the wall's response remains linear elastic before cracking drift ratio i.e. $\Delta_{FME} = \frac{1}{H} \frac{F_{FME}}{K}$ where K and F_{FME} are wall's stiffness and FME strength, respectively which are determined from Yekrangnia et al. (2017a, b). The spectral acceleration which induces inertial force equal to F_{FME} is shown by horizontal dashed lines denoting $S_{a-FME} = \frac{F_{FME}}{M}$ where M is the wall's total mass. The PGA related to S_{a-FME} which is denoted by PGA_{FME} is determined based on S_{a-FME} and natural period of the wall. For NS-S wall, $PGA_{FME} \cong S_{a-FME}$ because of very small natural period of the wall (refer to Fig. 9); whereas for EW-W wall, $PGA_{FME} \cong 0.5 S_{a-FME}$ from the average records sets shown in Fig. 10. The interesting finding is that at the intersection of Δ_{FME} and S_{a-FME} which is FME, the trend of correlation between EDP and IM changes to a smaller slope and larger scattering, both of which indicate response nonlinearity of the walls.

### 3.3.2 Fragility curves of constituent walls

The results of IDA from more than 78 thousand nonlinear time-history analyses based on 0.05 g increments were transformed into exceedance probabilities of certain performance levels i.e. FME and SME given an IM i.e. PGA following the procedure by FEMA P-58 and Baker (2015). It was assumed that the IDA results follow log-normal distribution which was fitted to the Cumulative Distribution Function (CDF) of the
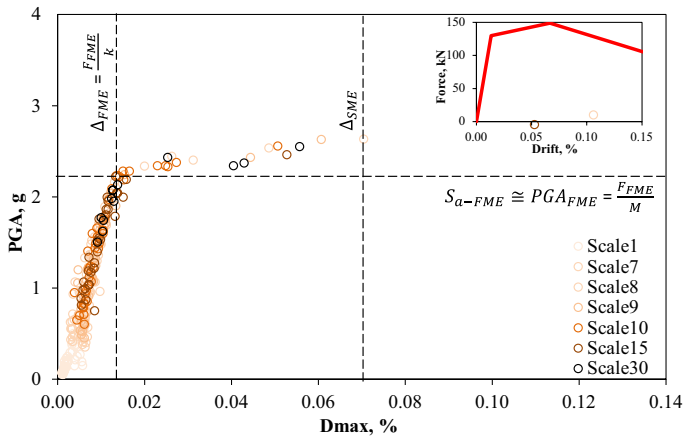
(a) NS-S Far-field set
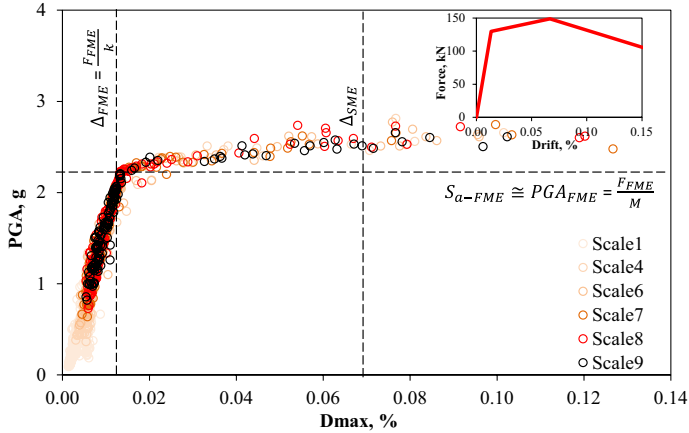
(b) NS-S Near-field set
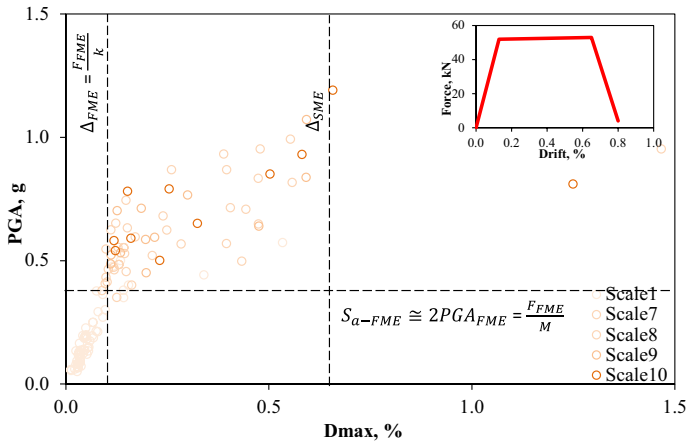
(c) EW-W Far-field set

Fig. 11 Correlation between EDP (maximum drift ratio) and IM (PGA) of two representative walls
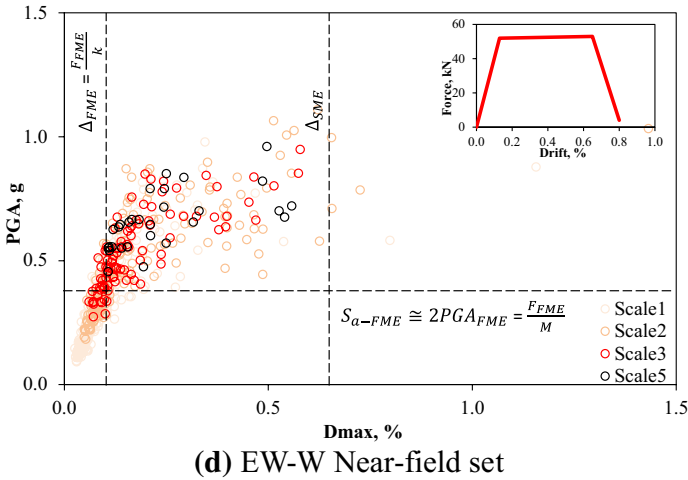
(d) EW-W Near-field set

Fig. 11 (continued)

results. The resulted fragility curves are shown in Fig. 12 for the representative walls. Each part of these figures consists of eight curves; half of these curves are related to CM walls (denoted by solid lines) and the other half are associated with the corresponding URM walls (shown by dashed lines). Also, one half is related to far-field set of ground motions (denoted by thin lines) and the rest of the curves show the near-field set results (represented by thick lines). There are two damage states considered in these figures i.e. FME (shown by green lines) and SME (represented by red lines); each of which includes half the fragility curves. Although NS-S walls carry no vertical loads from the roof, they are the only lateral load-bearing structural elements in the considered building in NS direction. Consequently, the total roof mass of each classroom (half roof mass from each adjacent classroom) is assigned to these walls for determination of their fragility curves.

The results of Fig. 12 are as follows; in part (a) there is no significant difference between the performance of CM and URM walls in both FME and SME damage states. This is mainly because the wall itself dominates the behavior of the CM wall and the wall has considerably larger stiffness and capacities than the ties which itself is originated from the length and the large vertical load carried by this wall. However, this is not the case for EW-W and NS-S (part (b) and part (c) of Fig. 12) in which the unconfined wall because of either having short length (part (b)) or having negligible vertical loads (part (c)) benefits hugely from the effects of the confining ties. This relative improvement in lateral response of EW-W and NS-S was also observed in the results of Fig. 9. The PGA related to the 50th percentile of exceedance probability of FME level is 0.15 g and 0.45 g for EW-W and NS-S having URM and CM walls, respectively which shows 200% improvement in seismic performance of these walls. Moreover, the corresponding PGA of SME level is 0.20 g and 0.55 g for NS-S having URM and CM walls, respectively which indicates an improvement of 175% in this level. The same conclusion from 90% performance improvement of SME level thanks to walls confinement can be made for EW-W. Note that in some fragility curves related to FME, the exceedance probability of CM is slightly larger than that of the corresponding URM wall. This is
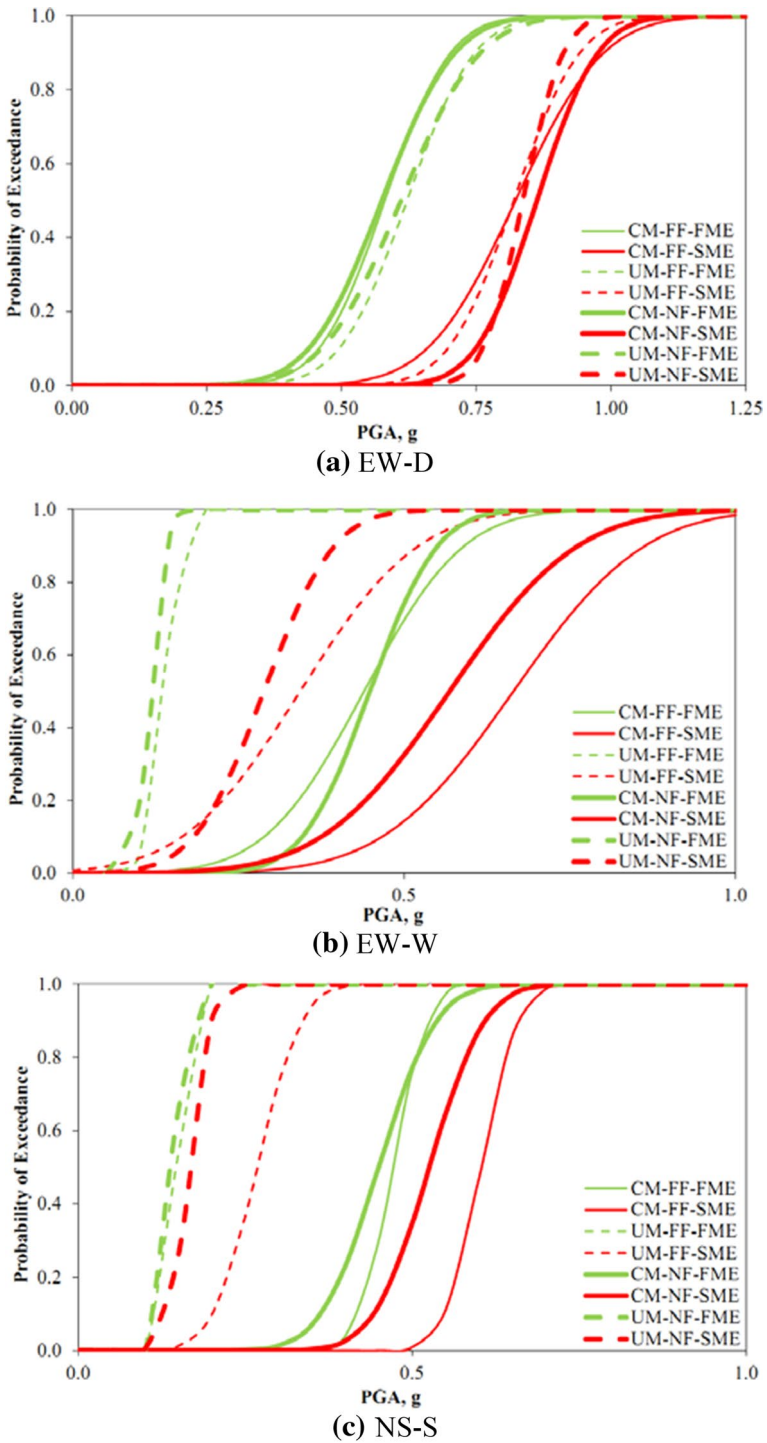
(a) EW-D

(b) EW-W

(c) NS-S

Fig. 12 Fragility curves of the considered representative masonry walls **a** Providing integrity **b** Providing rigidity

because the URM wall corresponding to CM, the length of confining ties was assumed to be also replaced with masonry wall (based on the assumption of constant walls' gross length), leading to slight increase in cracking strength.

Another observed feature for these curves is the dispersion of the results which is higher for SME level compared to FME level. This behavior has also been observed in Fig. 11 in which scattering of the results significantly increases from FME to SME. This is due to the fact that each considered model is at the verge of experiencing nonlinear behavior when reaching FME level; hence the linear-elastic response of the models contributes to determination of the fragility curves for FME level. However, the results related to SME level are based on the more sophisticated nonlinear behavior i.e. the assigned hysteretic rule for each wall. As a result, different structural parameters play a part in response determination and accordingly, more strong motion parameters in the applied earthquake records become more important. Consequently, weaker correlation exists between the EDP (maximum drift ratio) and the IM (PGA). For the same reason, the difference between the results related to far-field and near-field sets is more pronounced in the SME level compared to FME level. As can be seen, the former set leads to up to 0.10 g higher PGA associated with a considered exceedance probability. In other words, the considered walls show less capacity when subjected to near-field seismic actions. For example, the PGA causing SME level damages in EW-W associated with 50% probability of exceedance is 0.57 g and 0.67 g, respectively for near-field and far-field set; hence the former set, although scaled the same as the latter set, imposes larger seismic demands on the wall and hence, reduces the IM associated with SME by more than 17%.

3.3.3 Fragility curves of representative classroom

It can be claimed that the behavior of the selected school building is very similar to the behavior of the representative classroom having the walls shown in Fig. 7 because of the symmetrical plan of the building in both directions and also its classroom-based modular form. When it comes to the roof system of Iranian masonry buildings, they are either jack-arch roof or filler-joist, both classified as flexible diaphragms. However, Standard 2800, 2005 recommends providing these roofs with integrity by means of adding diagonal strips as shown in Fig. 13a. However, in many cases, the roof of these buildings is made rigid, albeit in in-plane direction, by casting a reinforced concrete layer on it (see Fig. 13b).

As schematically shown in Fig. 14a, the parallel walls in the representative classroom with rigid diaphragm experience equal top lateral displacements. However, these walls in the representative classroom with flexible diaphragm have independent degrees of freedom and hence, they should be evaluated separately (Fig. 14b).

3.3.3.1 Flexible diaphragm In order to derive fragility curves of the representative classroom with flexible diaphragm in EW direction, a combination of the results of part (a) and part (b) of Fig. 12 should be used. For this purpose, it is assumed that reaching a certain level of damage by either of the two load-bearing walls i.e. EW-D and EW-W leads to experiencing that particular level of damage in the classroom. As a result, the probability of exceedance of a certain level of damage in the representative classroom with flexible diaphragm in EW direction can be expressed as Eq. (1). It can be concluded from this equation that when diaphragm is flexible, the walls act independently and failure of at least one wall will lead to the failure of the whole system.
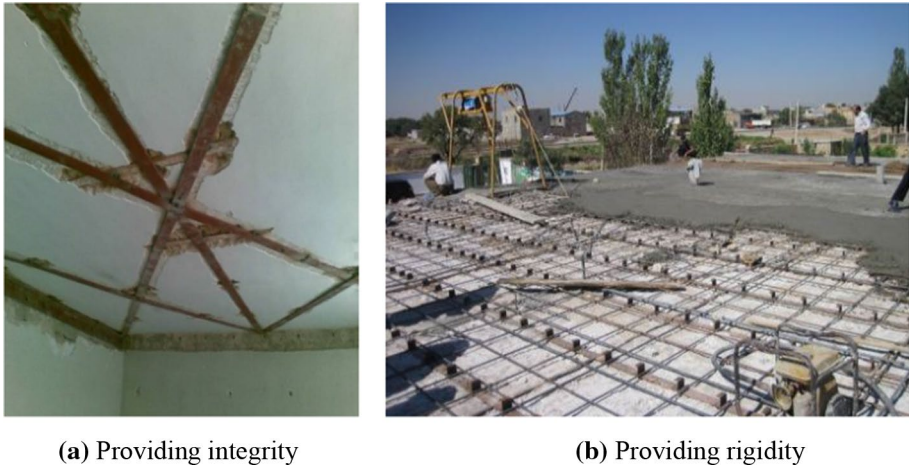
(a) Providing integrity   **(b)** Providing rigidity

Fig. 13 Practiced roof retrofit measures for Iranian masonry school buildings **a** Rigid Diaphragm **b** Flexible Diaphragm

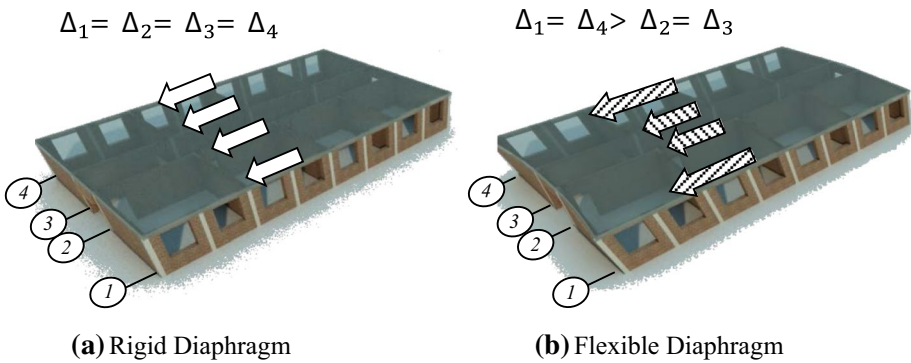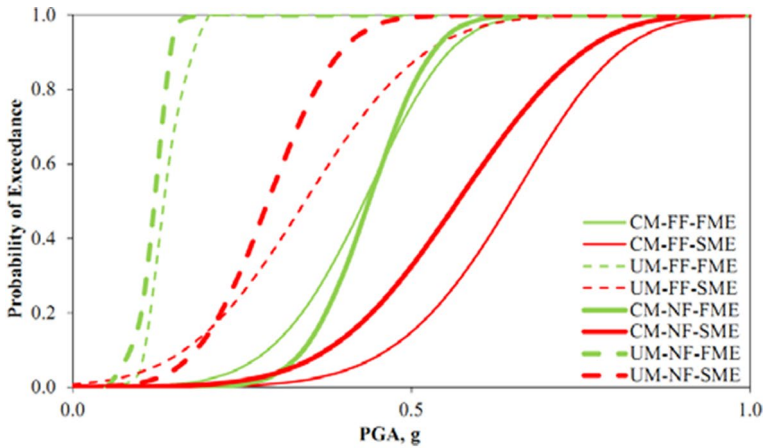**(a)** Rigid Diaphragm   **(b)** Flexible Diaphragm

**Fig. 14** Walls' deformation based on EW seismic loading demand **a** Flexible Diaphragm **b** Rigid Diaphragm

$$F_{DS_i}(\Delta) = \Phi\left(\frac{\ln\left(\frac{\Delta}{\Delta_m}\right)}{\beta}\right) = 1 - \prod_{j=EW-D}^{EW-W}(1 - P_j[DS \geq DS_i | EDP = \Delta]) \qquad (1)$$

$DS_i = FME \text{ and } SME, \Delta = Drift ratio.$

where Φ signifies the lognormal cumulative distribution function, Δ_m and β denote the median and the logarithmic standard deviation of the distribution, respectively. Note that according to this method, it is not necessary to perform additional analyses on model representing classroom with flexible diaphragm and the results of constituent walls of the classroom is put together in obtaining the fragility curves. The fragility curves of the representative classroom with flexible diaphragm in EW direction are shown in part (a) of Fig. 15.

(a) Flexible Diaphragm
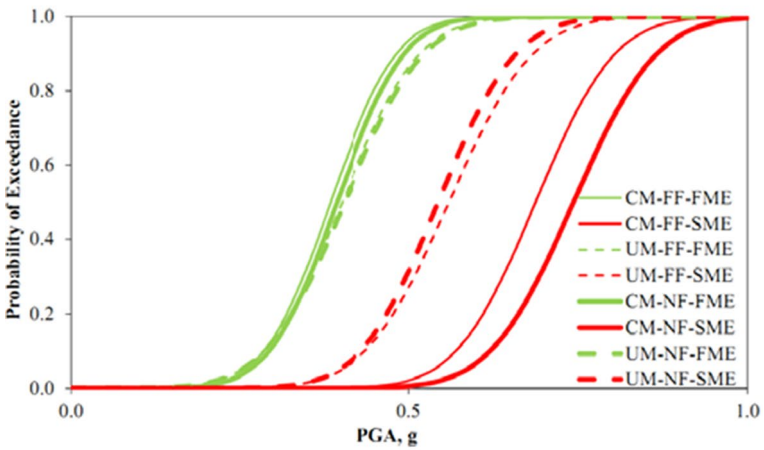
(b) Rigid Diaphragm

Fig. 15 Fragility curves of the considered representative classroom in EW direction

The notations used in this figure are similar to those in Fig. 12. As can be seen, the curves are comparable with the curves related to EW-W wall shown in Fig. 12b. This relative similarity is originated from the fact that EW-W is weaker than EW-D and because the walls act independently due to flexibility of the diaphragm, EW-W determines the response of the classroom. Note that the fragility curves of the representative classroom with flexible diaphragm in NS direction exactly duplicate the curves related to Fig. 12c for NS-S because this wall is the only wall contributing in response of the building in NS direction.

3.3.3.2 Rigid diaphragm Since the top displacements of the parallel walls are equal in the representative classroom with rigid diaphragm, its behavior can be reduced to a simple paralleled spring model which is a combination of EW-D and EW-W walls with the backbone force–displacement curve shown in Fig. 16. The curves in this figure are simply the summation of the resisting force of a single EW-D wall and two EW-W walls (since there

Fig. 16 Force–displacement curve of the representative classroom in EW direction with rigid diaphragm (Stiffness = 248 MN/m, Mass = 27.9 ton, Natural period = 0.07 s) **a** Seismicity of Central Alborz region **b** Location of masonry school buildings and V_{s30}
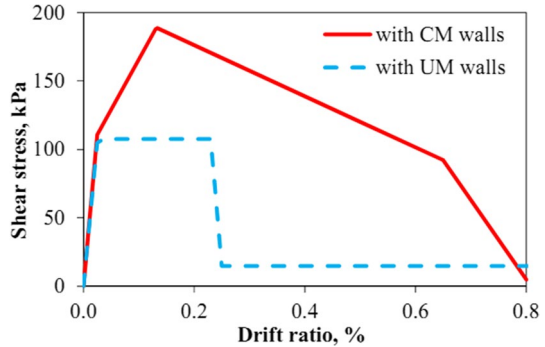
are two adjacent walls with window opening in each classroom; refer to Fig. 7) in EW direction at each lateral drift ratio. Also, doubling the force level at each drift of NS-S wall (Fig. 9) leads to the force–displacement curve of the representative classroom in NS direction because it constitutes two identical walls in this direction (Fig. 7). When regarded in the whole building, the representative classroom with rigid diaphragm cannot experience any torsion in its plan thanks to the roof boundary condition and symmetry of the building's plan. Nonetheless, if this classroom were analyzed as an isolated building, it would experience considerable torsion because of difference in stiffness of EW-D and EW-W as parallel walls (see Fig. 9). Consequently, contrary to the case of flexible diaphragm, it is necessary to perform additional IDA on new models with parallel springs (by summation of the force in force–displacement curves at each displacement for parallel walls in each direction) in order to obtain the fragility curves for the representative classroom with rigid diaphragm.

The fragility curves of the representative classroom with rigid diaphragm in EW direction are shown in part (b) of Fig. 15. Comparing the results of part (a) and part (b) of this figure indicates the ability of rigid diaphragms in reducing seismic vulnerability of masonry buildings. For example, for the representative classroom having CM walls, the PGA related to the 50th percentile of exceedance probability of SME level is 0.57 g and 0.72 g for cases with flexible and rigid diaphragm, respectively which shows 26% improvement in seismic performance of the considered classroom. The corresponding PGA for the classroom having URM walls are 0.30 g and 0.55 g for cases with flexible and rigid diaphragm, respectively, which indicates an improvement of 83% thanks to providing the roof with rigidity. This higher improvement of the results in the classroom with URM walls compared to that with CM walls is due to superior response characteristics of CM walls compared to URM walls which results in less sensitivity of these walls to the details of the roof. Note that the fragility curves of the representative classroom with rigid diaphragm in NS direction exactly duplicate the curves related to Fig. 12(c) for NS-S because this wall is the only wall which determines the response of the building in NS direction.

4 Scenario-based risk assessment: a case study of Tehran

In this part, a scenario-based risk assessment is conducted on a number of masonry school buildings. In order to perform seismic risk assessment, two components of risk i.e. seismic hazard (demands) and seismic vulnerability in the form of fragility curves should be

determined. First, seismic demands are determined by considering scenarios with different magnitudes for all the major adjacent faults of the target site. Then, the results of the previously-performed IDA are utilized to determine the seismic vulnerability of the considered school buildings.

Among different Iranian provinces, the Greater Tehran as the capital has the largest population of around 12 million people. The city is located in the vicinity of three active major faults, namely;

(1) The Mosha; a reverse fault dip-ping north ~ 175 km long at the southern edge of the Alborz mountains. It has been the cause of big historical earthquakes with magnitudes of over 6.5 in Anno Domini (AD) 958 (surface magnitude (Ms) ~ 7.7), AD 1665 (Ms ~ 6.5) and AD 1830 (Ms ~ 7.1) (Berberian and Yeats 2001).
(2) The North Tehran; which lies north and west of Tehran with an estimated length of 110 km. The focal mechanism of the North Tehran Fault is thrust with a component of left-lateral strike-slip motion (Nazari 2006). It has been the main cause of magnitude of Ms ~ 7.1 and Ms ~ 7.3 during 855–856 and 1177, respectively (Panahi et al. 2014).
(3) The Rey; which comprises North and South Rey which are 20.0 and 16.5 km, respectively. The occurrence of the historical earthquakes of 855 (Ms ~ 7.1), 864 (Ms ~ 5.3), 958 (Ms ~ 7.7) and 1177 (Ms ~ 7.2) could be the result of these faults' movements (Panahi et al. 2014).

Consequently, Tehran has one of the highest seismic risks both in Iran and even in the Middle East and hence, is considered as the target city for risk assessment. The seismic activity of the Central Alborz region and location of masonry school buildings in Tehran together with the average shear wave velocity at the 30 m depth (V_{s30}) and the three aforementioned faults are shown in Fig. 17. It is noted that there are 706 masonry school buildings in Tehran which as shown, most of them are located in the southern parts of the city. In the northern part which includes more recently-developed regions, the majority of school buildings are either steel or reinforced concrete frame structures.

4.1 Hazard assessment

The PGA distribution in Tehran based on three scenarios of Moment magnitude (M_w) = 5.5, 6.5 and 7.5 for the three adjacent faults is shown in Fig. 18. The attenuation
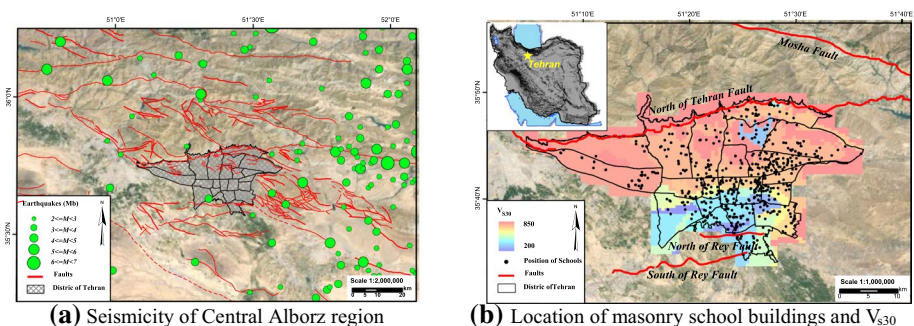

(a) Seismicity of Central Alborz region   **(b)** Location of masonry school buildings and V_{s30}

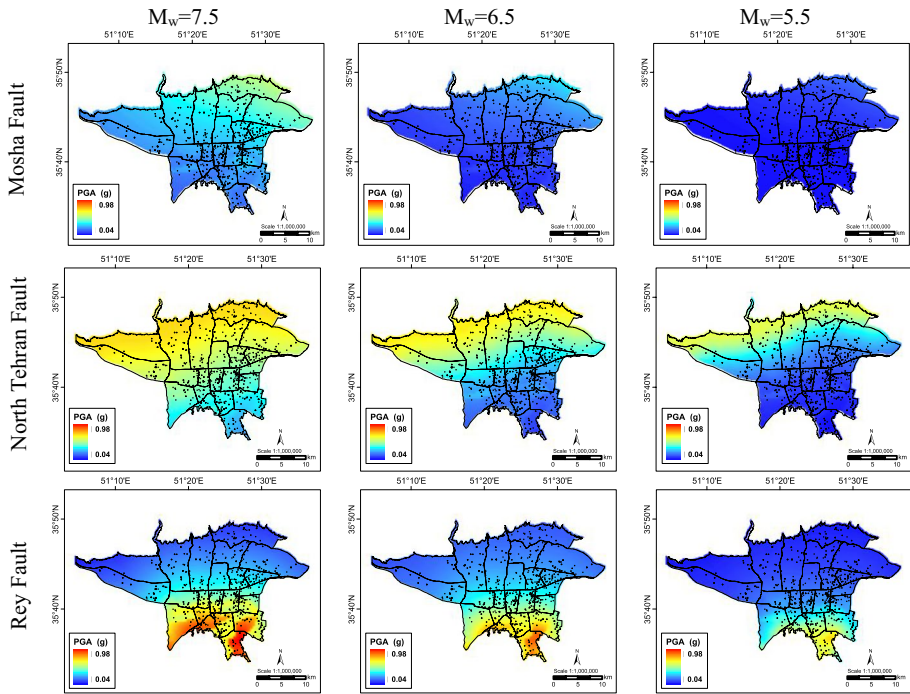**Fig. 17** Seismicity of Central Alborz and coordinates of masonry school buildings in Tehran

Fig. 18 Attenuated PGA (g) based on three scenarios for three adjacent faults in Tehran

relation proposed by Campbell and Bozorgnia 2003 is utilized which can properly account for the near-source seismic actions. The used attenuation relation is universal and hence, can be used herein. As observed, the Rey fault results in the highest PGA's according to the utilized attenuation relation which is originated from soft soil conditions in southern parts of Tehran.

4.2 Vulnerability assessment

In this part, a representative single-story masonry school building, consisting of 10 identical classrooms with the total area of 600 m² is considered for performing vulnerability assessment. The plan and the walls' characteristics are shown in Figs. 7, 9, respectively. After consulting with several contractors of Organization for Development, Renovation and Equipping of Schools in Iran (DRES) as the only organization responsible for construction and retrofit of school building throughout Iran, the average demolish-reconstruction cost for this school building is assumed $285,000 with the unit cost of $475/m². Note that all the non-structural parts including walls' granite finishing, flooring, doors, windows and heating–cooling system has been included in this unit cost; however, non-structural parts are considered as dependent parts to the structural parts and therefore no separate fragility function is assigned to them. Moreover, the average required time for demolish-reconstruction of the considered building is taken as 180 days. By assuming 30 students in each classroom, the total population of the considered school building is 300. The assumed
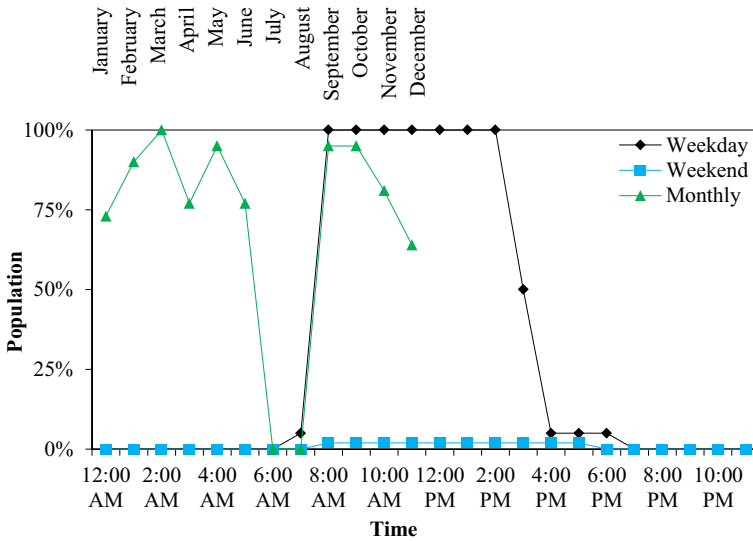
Fig. 19 Population model of the representative school building

population model which is accordant to the Education (k-12) (FEMA-395 2002) category is shown in Fig. 19.

　　Life cycle costs due to seismic hazards that may occur during the life time of a structure are usually categorized as the damage repair cost, loss of contents, loss of rental cost, loss of income cost, the cost of injuries and fatalities (Wen and Kang 2001; Mitropoulou et al. 2010). In this study, since the considerable variability of school contents, loss of contents has been excluded from the cost calculations. Furthermore, since most of the school buildings are public sector and belongs to the Iranian ministry of education, there is no loss of rental when the building is damaged. Loss of income is also not applicable to school buildings because they are used for educational purposes. Nonetheless, the costs associated with loss of use, loss of education, downtime, and also rental cost (renting other buildings as temporary schools) can be significant in many other cases and should be considered. These costs are also excluded in this study because they vary a lot and are hard to quantify. Also, solutions including using shelters and portable, prefabricated rooms installed in the yard of schools and dividing and transferring affected students to other schools in the neighborhood eliminate the aforementioned costs. Values of resulting EDP's can be replaced by related cost components using formulas in Table 4. In this table, unit damage repair costs are a function of structural component i.e. the three representative walls and the proposed drift-based performance levels i.e. FME and SME. These costs are shown in the first row of Table 5. The injury costs are calculated based on the multiplication of several components which are as follows. (1) The injury cost per person which varies a lot based on the type and extent of injury and a mean value of \$17.5 k is considered for it in this study. (2) The affected floor area which depends on each of the structural component damage and is presented in the third row of Table 5. For example, the affected floor for EW-D is half of the classrooms area because this wall is parallel with EW-W and carries approximately half of the dead and live loads. As a result, all the EW-W walls in the representative building attribute to 50% of the building's total area. (3) The occupancy rate which is based on the assumed population model is shown in Fig. 19. (4) The expected injury rate which as

Table 4 Itemized cost calculations

Cost component	Formula	Cost range	Considered cost
Damage repair	Unit repair cost×number of units×mean damage index	Varies (see Table 5)	Varies (see Table 5)
Downtime	Income rate×gross leasable area×down time	A proper replacement should be provided by DRES	–
Injury	Injury cost per person×affected floor area×occupancy rate×expected injury rate	($0.5 k~$135.0 k*) /person**	$17.5 k/person
Death	Human fatality cost per person×affected floor area×occupancy rate×expected death rate	($22.5 k~$45.0 k) /person**	$35.0 k/person

*Very rare in case of complete paralysis; **According to Iranian judicial system

Table 5 Expected consequence functions (assumed log-normal distributions with b = 0.1)

Wall	EW-D		EW-W		NS-S	
	FME	SME	FME	SME	FME	SME
Repair cost	$5.3 k	$7.9 k	$2.6 k	$3.9 k	$3.9 k	$5.9 k
Repair time	6 days	9 days	3 days	5 days	5 days	7 days
Non-collapse injury rate (Normalized affected populated area)	0.1 (50%)	0.2 (50%)	0.1 (50%)	0.2 (50%)	0.1 (100%)	0.2 (100%)
Non-collapse death rate (Normalized affected populated area)	–	0.1 (50%)	–	0.1 (50%)	–	0.1 (100%)

shown in the third row of Table 5, is considered 0.1 and 0.2 of all the constituent walls in FME and SME levels, respectively. The corresponding details are applied for calculation of death costs.

The utilized procedure is based on the framework for performance-based earthquake engineering proposed by PEER (Moehle and Deierlein 2004). Several sources of uncertainties in loss estimation can be characterized in this framework including uncertainties in earthquake hazard characteristics, development of an analytical model of the structure, the construction quality and material characteristics (Basim and Estekanchi 2015). A Monte Carlo approach is implemented to apply the integration of statistically compatible simulated demand data with a limited number of analyses. As mentioned, a scenario-based approach is considered to account for three different possible major earthquakes from the three adjacent faults in Tehran. To account for the uncertainties in loss calculation, a fragility specification is assigned for each vulnerable component in the form of a series of distinct damage states which are the same as those previously introduced for the constituent walls for FME and SME damage states (see Fig. 11). Each damage state is associated with a set of consequences consisting of a probable repair action with associated repair cost and casualty rate. For each damage state, a lognormal distribution is considered that indicates the conditional probability of incurring damage at a certain value of the imposed demand.

Although FEMA-P-58 (2012) provides components fragilities for many structural systems, there is no data available for CM buildings in this document. As a result, after consulting with several contractors and university faculties specialized in masonry buildings, the fragility groups associated with CM school buildings has been determined from the previous parts of this paper. The required information for these groups are based on the three representative walls, the damage states and the related fragilities, and also all the consequence functions including repair cost, repair time and non-collapse injuries and deaths. These values for each fragility group (which is referred to performance group because these groups experience similar seismic demands) are presented in Table 5 which has been previously introduced.

4.2.1 Uncertainties in demand parameters

For scenario-based assessment, a range of IM's related to negligible damage to collapse is considered namely from 0.10 g to 0.50 g for the considered URM school building model

and from 0.25 g to 0.70 g for the corresponding CM school building. The results of IDA on the representative masonry school building in two confined and unconfined states under near-field ground motions presented in the previous parts of this paper are utilized to predict median values and estimate dispersion of results.

Uncertainties in demand parameters including modeling uncertainty and ground motion variability are taken into account by proper judgmental assumptions found in FEMA-P-58, 2012. Modeling uncertainty (β_m) is used to account for the level of building definition and construction quality assurance (β_c), and the quality and completeness of the IDA models (β_q). In this study, we assume $\beta_c = \beta_q = 0.25$ based on averaged-quality results according to FEMA-P-58 (2012) which leads to $\beta_m = \sqrt{\beta_c^2 + \beta_q^2} = 0.35$. Record to record variability, β_{rGM} is implicitly obtained by considering a large number of Ground Motions (GM) set i.e. 266 here which is far larger than the recommended value of 30 according to FEMA-P-58 (2012). Also, ground motion variability, β_{GM} which takes into account the uncertainty in the shape and amplitude of the target spectrum and the values for ground motion spectral demand uncertainty in the utilized attenuation relationship is assumed 0.6 according to FEMA-P-58 which is in good agreement with the upper bound value found in Campbell and Bozorgnia (2003).

4.2.2 Fragility functions for collapse and residual story drift ratio

Building collapse is the main cause of earthquake casualties and economic loss. Assessment of collapse-induced damages requires the development of the building collapse fragility. Collapse fragility functions are used to determine the probability of collapse in different IM's. The probability of collapse is expressed as a lognormal distribution of PGA (as the selected IM here), defined by a median value and dispersion. Various methods of collapse assessment have been defined in FEMA-P-695 (2009). Since the experimental data related to the level of collapse of CM walls is very limited, it is practically impossible for the proposed models by Yekrangnia et al. (2017a, b) which were calibrated against several experimental results to precisely determine the level of collapse of these buildings. However, since the central-difference solution method has been utilized in this study, very large displacement demands can be numerically modeled without any limitations induced from convergence problems as for Basim and Estekanchi (2015). Consequently, the level of collapse has been assumed to be 1.5 times of the story drift ratio associated with SME. This value may be conservative as results of few shaking table tests on CM buildings show these structures can tolerate displacement demands much larger than the displacement associated with SME level (Tomaževič, and Gams 2012). For the selected GM set, this leads to median PGA of 0.92 g which is based on the minimum PGA value associated with the collapse of the a single component wall. A large value of dispersion of 0.6 is assumed for the log-normal distribution considering several uncertainties attributed to this performance level.

Once the collapse happens, a total building replacement cost is used as the induced cost. Besides, when the total cost of repair exceeds a threshold value or when the residual drift ratio exceeds a repairable limit, the building replacement is favored over its repair and consequently, the replacement cost is considered. Speaking of Iranian school buildings, a value of 30% of the replacement cost is considered as the threshold of justification for seismic retrofit projects by DRES. In the absence of a threshold, this value is also considered for post-earthquake decision making about replacement-repair; however, the assumed threshold is subjective and greatly depends on the post-earthquake circumstances in terms of

time and budget restrictions. For the residual drift, a tentative fragility is assumed with a lognormal distribution having a dispersion of 0.4 (FEMA P-58) and a median value of 0.15% residual story drift ratio based on few available in-situ test data (Yekrangnia et al. 2018) and post-earthquake field observations (Yekrangnia et al. 2017a, b). This value is half of the averaged drift ratio related to SME level for the three constituent walls. It is noteworthy that the residual drift criterion is independent to the collapse criterion.

4.2.3 Performance calculation

The probabilistic performance of the structure is calculated by generation of simulated demands based on the GM set results, collapse assessment and repairability, determination of damages and losses in terms of expected repair cost and time, casualties and collapse probability. To evaluate uncertainties and variability in building performance and related losses, a large number of demand sets (a set of IM values at each mean intensity level following certain distribution) are simulated for each intensity level (with 0.05 g interval) based on the statistical distribution of demands obtained from IDA; each representing a possible building response (FEMA-P-695 2012). In the next stage, for each simulated demand set, the consequences are determined by Monte Carlo method based on the assumed fragility and consequence functions. Each unique performance consequence related to one single simulated demand set is named a realization. For each realization, the occurrence time of day and day of year and the number of occupant people in the building at the time of seismic action are determined by random number generation. Following, the collapse occurrence is calculated by means of the collapse fragility function. If a realization results in the condition that neither collapse has occurred nor the residual story drift ratio exceeds the assumed threshold, the damaged structure is deemed to be repairable and the damage of each performance group is determined based on the provided fragility curves and consequence functions. Otherwise, the building total replacement cost will be used as the induced cost for that realization and the number of casualties is predicted based on the building population according to the population model and the considered collapse casualty rate. For example, a random number between 0 and 100 is generated for determination of collapse occurrence. According to the assumed distribution for collapse with the median of 0.92 g (as mentioned in part "Fragility functions for collapse and residual story drift ratio" in this paper), based on coin toss probability, if the generated number is less than or equal to 50 (out of 100) for that particular intensity level i.e. 0.92 g, the realization is considered to be encountered with collapse. The same procedure is followed for determination of other consequences. In scenario-based assessment, the aforementioned procedure is repeated for each intensity level. In this study, 1500 realizations are utilized for each intensity level to assess a range of possible outcomes. The assumed number of occurrences is sufficient to result in 2.4% variance in the results of a number of consecutive similar runs. The results of the PGA intensity equal to 0.65 g for the representative CM school building for each wall in terms of damage costs is depicted in Fig. 20. As can be seen, EW-D and NS-S contribute to the most damage costs because of their lower displacement capacity compared to EW-W (see Fig. 9) and large surface area which leads to larger repair cost compared to NS-S (see Table 5). Note that realizations from 750 to 1150 result in collapse of the building. Also, the building is deemed unrepairable due to excessive experienced residual drifts in realizations from 1151 to 1500 and as a result, the total building value (replacement cost) is considered for them which is shown by the upper horizontal dashed line. For realizations from 1 to 649, the damage costs for each of the constituent
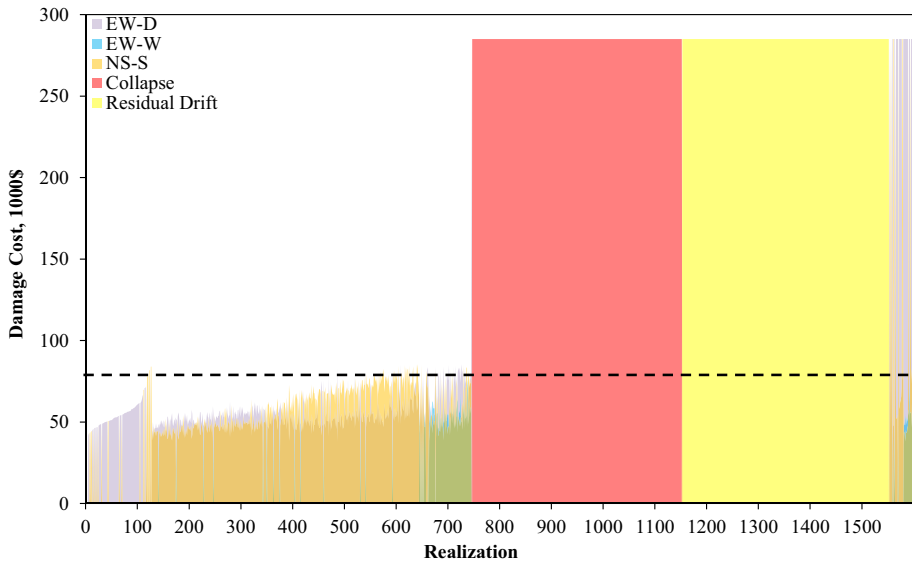
Fig. 20 Realizations of PGA = 0.65 g for the representative school building **a** Repair cost **b** Repair time **c** Injuries and deaths

walls set is not larger than the assumed threshold for replacement i.e. 30% of the replacement costs which is shown by the horizontal dashed line.

Probability of exceedance based on the considered intensities in terms of repair cost, repair time and casualties are calculated and the results are shown in Fig. 21. Part (a) of this figure indicates that if the PGA of a scenario at a given site is equal to 0.40 g, there is approximately 50% probability of exceedance of the tolerable threshold cost for repair of the building i.e. 30% of the replacement cost shown by a vertical dashed line. It is assumed if a CM school building experiences a PGA of less than 0.40 g, it is deemed to be repaired (because the exceedance probability of repair cost threshold at that IM is slightly larger than 50% which is assumed herein as a threshold for decision making about repair/reconstruction); otherwise, replacement of the damaged or collapsed building with the new building identical to the previous one is the option based on the existing limitations i.e. collapse, residual story drifts and the 30% loss threshold. The 50% of exceedance probability at the tolerable threshold cost, which correlates with PGA = 0.40 g, is a subjective level for decision making and lower exceedance probabilities related to lower PGA's may be considered as a benchmark for decision about demolish-reconstruction or repair of CM school buildings in the scope of risk-aversion. The considered benchmark PGA is because the costs probability of exceedance of the considered CM building insignificantly changes from PGA of 0.25 g to 0.40 g. The repair time also shows no significant increase from 0.25 g to 0.40 g. As a result, the upper bound of these intensities is considered as the benchmark. To be more specific, uncertainty in the costs is dealt with by "accepting" a level of uncertainty at the cost threshold and considering two cases i.e. demolish/reconstruction and repair. With this approach, each building, depending on the experienced PGA, is categorized as either of the two aforementioned cases and the related costs are calculated. If the building has to be reconstructed, its area is considered for determination of the resulted cost. If it needs to be repaired, its area and the integral of probability curve

Fig. 21 Probabilistic risk assessment of the representative CM school building

(a) Repair cost

(b) Repair time

(c) Injuries and deaths
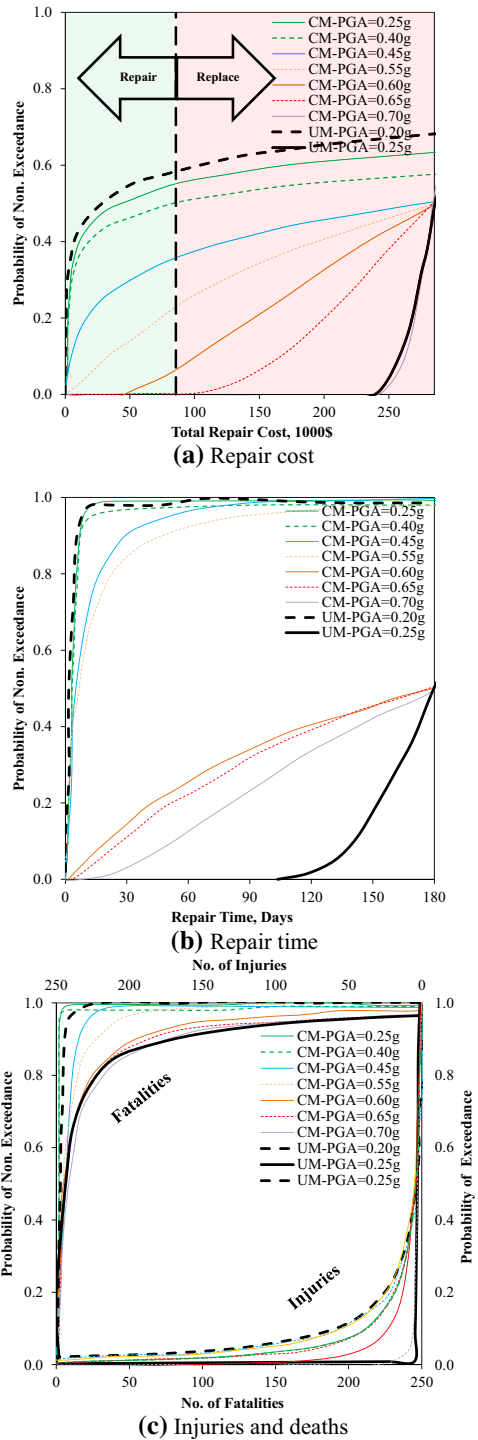
for that particular experienced PGA (if the PGA curve is not found in Fig. 21, its values are calculated using interpolation of the available curves) which leads to the expected value of the cost are taken into account for determination of the resulted cost. By considering 42% probability of exceedance of the tolerable threshold cost for repair, the representative URM school building has to be replaced when PGA > 0.20 g. Note that for the curve related to PGA = 0.25 g, the probability of exceedance for the tolerable threshold is 100%. This means the considered URM building is very sensitive to even small increase in PGA (as IM). This behavior is also observed in Fig. 12 when comparing fragility curves of URM walls with those of CM walls; the former has lower dispersion and hence narrower distribution shape. This sensitivity of URM buildings to PGA has been previously observed in Iranian earthquakes. As an example, Moghaddam (Moghaddam 2015) reported during Manjil earthquake in 1990, URM buildings which were approximately 10 km from the epicenter were severely damaged or collapsed. However, URM buildings with similar material quality and construction details experienced slight damages because they were located in villages approximately 15 km from the epicenter, which means they experienced slightly lower PGA. The same goes for repair time and the casualties which clearly prove performance superiority of the CM over the URM school building. It is noted that the probabilities of occurrence of certain level of damage cost, repair time and casualties is very close for CM between intensities 0.25 g and 0.40 g. The abrupt increase in probability of exceedance in these parameters from 0.40 g to 0.45 g is originated from the abrupt increase in the EDP at the FME level, as shown in Fig. 11. Based on the results of Fig. 21 part (a) for the representative CM school building, the damage costs for different considered scenarios, assuming all the masonry school buildings in Tehran as CM, are shown in Fig. 22. Note that in determination of the costs associated with each site (school building), two parameters are considered: (1) The experienced PGA based on which the cost is determined for the representative building. If the experienced PGA is larger than 0.40 g and 0.20 g, the total replacement cost is considered for that particular CM and URM building, respectively; otherwise, the expected value of damage cost is determined based on the probability distribution according to Fig. 21 part (a); (2) The area of school building based on which the resulted cost for the representative building is linearly scaled up or down depending on the ratio of school building area to that of the representative school building (600 m^2). As seen in this figure, the damages are concentrated at the northern and central parts of Tehran from the assumed scenario of $M_w = 7.5$ from North Tehran fault; however, only northern part of Tehran is hugely affected by a scenario of $M_w = 6.5$ from the same fault. The same observation can be made in $M_w = 7.5$ and $M_w = 6.5$ for Rey fault. As a result, $M_w = 7.5$ for both of these faults results in a numerous damaged school buildings and hence considerable increase in the overall damage costs.

The results of the seismic assessment of masonry school buildings in Tehran in terms of the grand total damage cost for each of the three considered earthquake magnitude from the three faults and the related displaced students (students whose school building needs either repair or replacement) are shown in Fig. 23. Note these nine scenarios are repeated for two separate cases by assuming all masonry school buildings in Tehran as CM and URM; in both of these cases, the school buildings are assumed to be unretrofitted single-story buildings. This assumption is not correct since the majority of vulnerable masonry school buildings in Tehran have been shotcreted or demolished and reconstructed. Also, these buildings are either single-story, two- or three-story; however, it is ideally assumed that all the masonry school buildings are single-story. These idealizations are made in order to present an illustrative example of the risk assessment of single-story masonry school buildings in Tehran with the emphasis of positive effects of confinement on the seismic performance
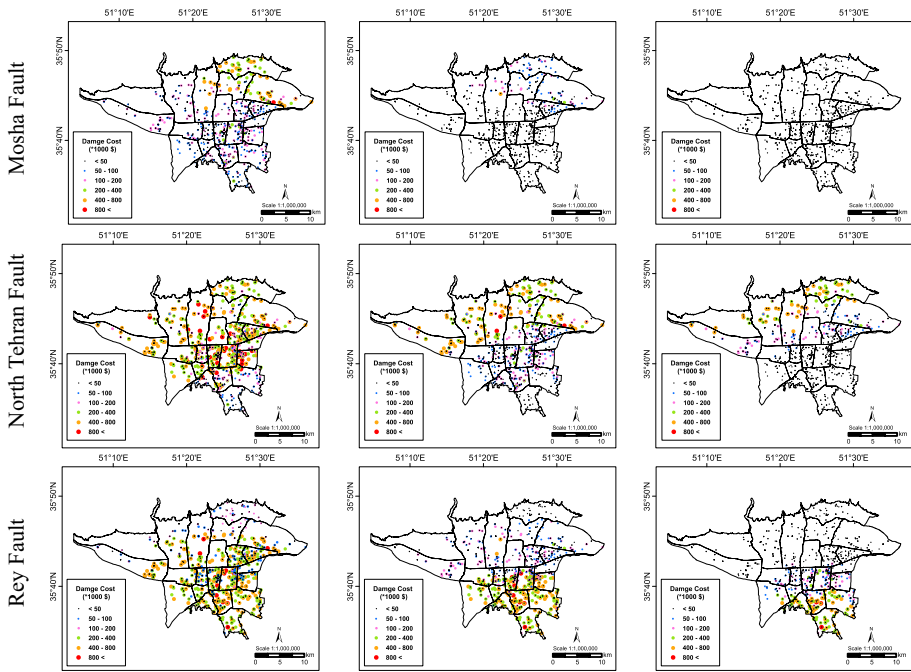
Fig. 22 Damage costs for different scenarios of CM school buildings in Tehran **a** Damage cost **b** Number of displaced students

of these buildings. Figure 23 contains important findings which indicate the huge reduction of damage costs and number of displaced students thanks to the seismic performance improvement of CM school buildings over URM ones. Based on this figure and assuming all school buildings as URM, the damage costs are maximum (replacement of all masonry school buildings in Tehran) when $M_w = 7.5$. Comparing the costs for CM school buildings in $M_w = 7.5$ for Rey and North Tehran faults with those of URM ones, it is concluded that the damage severity is so high that CM buildings leads to marginal reduction in the overall costs; however, this is not the case in $M_w = 7.5$ for Mosha fault. Because this fault is located far from Tehran compared to the other two faults, the induced seismic hazards from this fault for a particular magnitude is lower than those for Rey and North Tehran faults; hence, the improvement of CM school buildings over URM ones can be easily identified. The real benefit of performance improvement of CM school buildings is seen for $M_w = 6.5$ and $M_w = 5.5$ scenarios which in some cases leads to reduction of damage costs to less than half of those related to URM school buildings. The same conclusions can be made for the results presented in part (b) of Fig. 23 for the number of displaced students.

5 Conclusions

Seismic performance of a representative single-story masonry school building in Tehran was assessed using analytical modeling and through incremental dynamic analyses. Fragility curves were derived for each of the constituent walls of the building both in unconfined
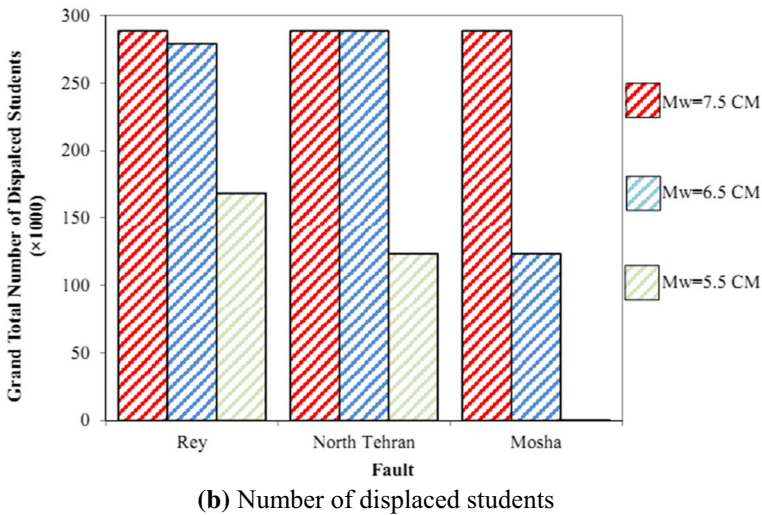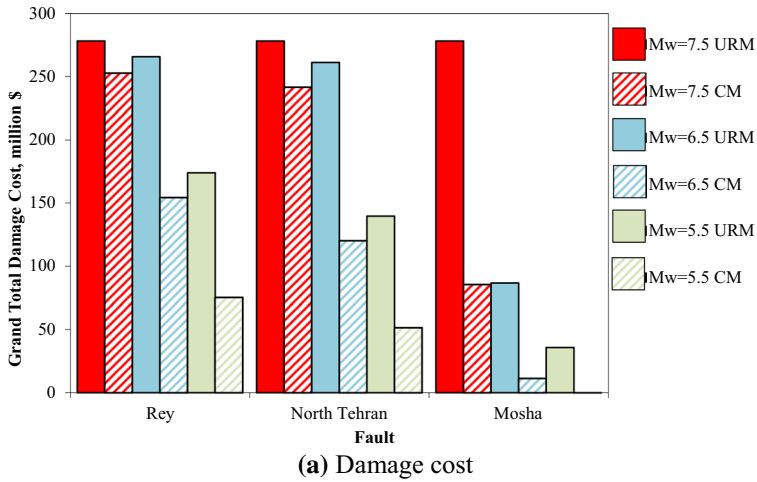
(a) Damage cost

(b) Number of displaced students

Fig. 23 Overall cost consequences in Tehran

and confined states. Also, response assessment of the modular classroom under various roof conditions was made by determination of fragility curves. Both far-field and near-field ground motion sets were taken in to account. The results of IDA indicated that PGA related to the 50th percentile of exceedance probability of FME level for the considered walls increases 200% thanks to adding ties to the walls and providing confinement. This increase in the median PGA is from 90 to 175% in the SME level depending on the wall i.e. NS, EW-D and EW-W. It was observed that PGA related to the 50th percentile of exceedance probability of SME level for CM and URM classroom is 26% and 83% larger by providing the roof with rigidity. Also, the near-field records cause a decrease of up to 17% in the PGA related to the 50th percentile of exceedance probability compared to that of the far-field records; causing severer seismic demands on the considered building. Utilizing the results of the nonlinear time-history analyses and the available data of masonry school buildings in Tehran, a scenario-based risk assessment of these school buildings was carried out. It

was shown that improving seismic performance of masonry school buildings in Tehran by providing confinement to the walls can lead to over \$100 million reduction in the damage costs under scenarios $M_w = 5.5$ and 6.5; whereas this undertaking is not of much effect for $M_w = 7.5$ from North Tehran and Rey faults. The findings in this study can be of direct use for disaster management of masonry school buildings in Tehran and other similar cities.

The results of this study are limited to single-story masonry buildings. The masonry buildings with higher number of stories may be more vulnerable against seismic actions compared to the corresponding single-story buildings (Quiroz and Maruyama 2017). As stated by Azizi-Bondarabadi et al. (2016), the method can be used for all schools in Iran due to their similar architectural and structural configurations and construction techniques. Moreover, it can be employed to provide fragility curves for typical masonry residential buildings, given the building types considered.

References

Amiri GG, Dana FM (2005) Introduction of the most suitable parameter for selection of critical earthquake. Comput Struct 83(8):613–626

ASCE (2005) Minimum design loads for buildings and other structures (ASCE/SEI 7–05). American Society of Civil Engineers, Reston, VA, USA

ASCE (2013) Seismic rehabilitation of existing buildings (ASCE/SEI 41–13). American Society of Civil Engineers, Reston, VA, USA

Azizi-Bondarabadi H, Mendes N, Lourenço PB, Sadeghi NH (2016) Empirical seismic vulnerability analysis for masonry buildings based on school buildings survey in Iran. Bull Earthq Eng 14(11):3195–3229

Baker JW (2015) Efficient analytical fragility function fitting using dynamic structural analysis. Earthq Spectra 31(1):579–599

Bakhshi A, Ahmadi MH, Yekrangnia M (2014) Development of fragility curves of confined masonry buildings. 9th International masonry conference, Guimaraes, Portugal

Basim MC, Estekanchi HE (2015) Application of endurance time method in performance-based optimum design of structures. Struct Saf 56:52–67

Benjamin JR, Cornell CA (1970) Probability, statistics, and decision for civil engineers. McGraw-Hill, New York, USA

Berberian M, Yeats RS (2001) Contribution of archaeological data to studies of earthquake history in the Iranian plateau. J Struct Geol 23:563–584

Bommer JJ, Magenes G, Hancock J, Penazzo P (2004) The influence of strong-motion duration on the seismic response of masonry structures. Bull Earthq Eng 2(1):1–26

Campbell KW, Bozorgnia Y (2003) Updated near-source ground-motion (attenuation) relations for the horizontal and vertical components of peak ground acceleration and acceleration response spectra. Bull Seismol Soc Am 93(1):314–331

Chiou B, Darragh R, Gregor N, Silva W (2008) NGA project strong-motion database. Earthq Spectra 24(1):23–44

Dhakal RP, Singh S, Mander JB (2007) Effectiveness of earthquake selection and scaling method in new zealand. Bull N Z Soc Earthq Eng 40(3):160–171

Dolatshahi KM, Yekrangnia M (2015) Out-of-plane strength reduction of unreinforced masonry walls because of in-plane damages. Earthq Eng Struct Dynam 44(13):2157–2176

Dolatshahi KM, Aref AJ, Yekrangnia M (2014) Bidirectional behavior of unreinforced masonry walls. Earthq Eng Struct Dynam 43(15):2377–2397

Ebrahimian H, Jalayer F, Lucchini A, Mollaioli F, Manfredi G (2015) Preliminary ranking of alternative scalar and vector intensity measures of ground shaking. Bull Earthq Eng 13(10):2805–2840

EN 1052-3 (2002) Methods of test for masonry—Part 3: Determination of initial shear strength. European Committee for Standardization, Brussels

Fenves GL, Mazzoni S, McKenna F, Scott MH (2004) Open system for earthquake engineering simulation OpenSees. University of California, Berkeley, CA, USA, Pacific Earthquake Engineering Research Center

FEMA-395 (2002) Incremental seismic rehabilitation of school buildings (K-12). Federal Emergency Management Agency, Washington, D.C, USA

FEMA 461 (2007) Interim testing protocols for determining the seismic perfromace characterstics of structural and nonstructural components. Federal Emergency Management Agency, Washington, D.C., USA

FEMA 440 (2005) Improvement of nonlinear static seismic analysis procedures. Federal Emergency Management Agency, Washington, D.C., USA

FEMA P-440A (2009) Effects of strength and stiffness degradation on seismic response. Federal Emergency Management Agency, Washington, D.C., USA

FEMA-P-58 (2012) Seismic performance assessment of buildings. Federal Emergency Management Agency. Washington, D.C., USA

FEMA-P-695 (2009). Quantification of building seismic performance factors. Federal Emergency Management Agency, Washington, D.C., USA

Ghahari SF, Jahankhah H, Ghannad MA (2010) Study on elastic response of structures to near-fault ground motions through record decomposition. Soil Dyn Earthq Eng 30(7):536–546

Iranian code of practice for seismic resistant design of buildings (Standard 2800) (2015) Fourth Revision, Building and Housing Research Center, Iran (in Persian)

Jalayer F, Beck JL, Zareian F (2012) Analyzing the sufficiency of alternative scalar and vector intensity measures of ground shaking based on information theory. J Eng Mech 138(3):307–316

KhalafRezaei M (2012) Analytical and experimental evaluation of confined masonry walls retrofitted by shotcreting with ordinary and steel fibers concrete. MSc Thesis, Tarbiat Modares University, Tehran, Iran (in persian)

Kostov M, Koleva N (2007) Damage potential of the seismic strong motion. 8th pacific conference on earthquake engineering, Singapore

Lovon H, Tarque N, Silva V, Yepes-Estrada C (2018) Development of fragility curves for confined masonry buildings in Lima Peru. Earthq Spectra 34(3):1339–1361

Luco N, Cornell CA (2007) Structure-specific scalar intensity measures for near-source and ordinary earthquake ground motions. Earthq Spectra 23(2):357–392

Meli R, Brzev S, Astroza M, Boen T, Crisafulli F, Dai J, Farsi M, Hart T, Mebarki A, Moghadam AS, Quiun D, Tomazevic M, Yamin L (2011) Seismic design guide for low-rise confined masonry buildings. Confined Masonry Network, A Project of the World Housing Encyclopedia, EERI and IAEE, Oakland, CA, USA

Mitropoulou CC, Lagaros ND, Papadrakakis M (2010) Building design based on energy dissipation: a critical assessment. Bull Earthq Eng 8:1375–1396

Moehle J, Deierlein GG (2004) A framework methodology for performance-based earthquake engineering. 13th world conference on earthquake engineering and seismology (13WCEE), Vancouver, British Columbia, Canada

Moghaddam H (2015) Seismic design of brick buildings, 6th edn. Sharif University of Technology, Tehran, Iran

Mosalam KM, White RN, Gergely P (1997) Static response of infilled frames using quasi-static experimentation. J Struct Eng 123(11):1462–4169

Nazari H (2006) Analyse de la tectonique récente et active dansl'alborz central et la région de Téhéran: approche morphotec-toniqueet paléoseismologique, PhD thesis, University of Mont-pellier II

New Zealand standard structural design actions part 5: Earthquake actions (2004) (NZS1170.5), Wellington, New Zealand

Panahi M, Rezaie F, Meshkani SA (2014) Seismic vulnerability assessment of school buildings in Tehran city based on AHP and GIS. Nat Hazards Earth Syst Sci 14:969–979

Quiroz LG, Maruyama Y (2017) Seismic assessment of Peruvian confined masonry dwellings using fragility functions, 16th world conference on earthquake engineering and seismology (16WCEE), Santiago, Chile

Reinoso E, Ordaz M, Guerrero R (2000) Influence of strong motion duration in seismic design of structures. 12th world conference on earthquake engineering and seismology (12WCEE), Auckland, New Zealand

Rural houses specifications count (2003) Housing Foundation of Iran, Tehran, Iran

Sarrafi B, Eshghi S (2012) Experimental study on lateral strength of confined masonry walls. 15th world conference on earthquake engineering (15WCEE), Lisbon, Portugal

Shome N, Cornell AC, Bazzurro P, Carballo JE (1998) Earthquakes, records and nonlinear responses. Earthq Spectra 14(3):469–500

Tasnimi A (2004) The behavior of masonry walls constructed according to the Standard 2800. Building and Housing Research Center, Bulletin of research No 404, Tehran, Iran

Tomaževič M, Gams M (2012) Shaking table study and modelling of seismic behaviour of confined AAC masonry buildings. Bull Earthq Eng 10(3):863–893

Wen Y, Kang Y (2001) Minimum building life-cycle cost design criteria. II: applications. J Struct Eng 127:338–346

Yekrangnia, M, Mahdizadeh A (2009). URM Buildings and earthquake: in-depth evaluation of earthquake damages to URM buildings. Scientific report. Organization for Development, Renovation and Equipping Schools of I.R. Iran

Yekrangnia M, Bakhshi A, Ghannad MA (2017) Force-displacement model for confined masonry walls with shear-dominated failure mode. Earthq Eng Struct Dynam 46(13):2209–2234

Yekrangnia M, Mohammadi M (2017) A new strut model for solid masonry infills in steel frames. Eng Struct 135:222–235

Yekrangnia, M., Eghbali, M., Panahi, M., Zanganeh, S.Y., Beyti, M., and Hayatgheybi, S.V. (2017). A preliminary report on school buildings performance during M 7.3 Ezgeleh, Iran earthquake of November 12, 2017. Earthquake Engineering Research Institute (EERI)

Yekrangnia M, Aghababai A, Bakhshi A, Ghannad MA, Mirghaderi SR, Khanmohammadi M (2018) In-situ cyclic testing on a typical URM school building-Part II: the confined masonry building. 10th international masonry conference, Milan, Italy

Zhai CH, Xie LL (2007) A new approach of selecting real input ground motions for seismic design: the most unfavourable real seismic design ground motions. Earthq Eng Struct Dynam 36(8):1009–1027

Affiliations

Mohammad Yekrangnia[1] · Ali Bakhshi[2] · Mohammad Ali Ghannad[2] · Mahdi Panahi[3]

Mohammad Yekrangnia
yekrangnia@sru.ac.ir; m.yekrangnia@gmail.com

Mohammad Ali Ghannad
ghannad@sharif.edu

Mahdi Panahi
panahi2012@yahoo.com

[1] Department of Civil Engineering, Shahid Rajaee Teacher Training University, 16785-163 Tehran, Iran

[2] Department of Civil Engineering, Sharif University of Technology, 11155-9313 Tehran, Iran

[3] Geoscience Platform Division, Korea Institute of Geoscience and Mineral Resources (KIGAM), 124, Gwahak-ro Yuseong-gu, Daejeon 34132, South Korea